



Beyond HCHO/NO₂: Global Daily Maps of Net Ozone Production Rates and Sensitivities Constrained by Satellite Observations (2005–2023)

Amir H. Souri^{1,2*}, Gonzalo González Abad³, Bryan N. Duncan¹, Luke D. Oman¹

¹Atmospheric Chemistry and Dynamics Laboratory, NASA Goddard Space Flight Center, Greenbelt, MD, USA

²GESTAR II, Morgan State University, Baltimore, MD, USA

³Atomic and Molecular Physics (AMP) Division, Center for Astrophysics | Harvard & Smithsonian, Cambridge, MA, USA

* Corresponding author: a.souri@nasa.gov

Abstract. Previous studies on net ozone production rates (PO₃) and their sensitivities to precursors relied on limited in-situ data, often coarse and uncertain chemical transport models (CTMs), and ozone indicators like the formaldehyde-to-nitrogen dioxide ratio (FNR). However, FNR fails to fully capture PO₃'s complex relationships with pollution, light, and water vapor. To address this, we refine the satellite-based PO₃ product from Souri et al. (2025) with key advancements: (i) a deep neural network to parametrize high-dimensional non-linear ozone chemistry without the need for empirical linearization of atmospheric conditions, (ii) incorporation of water vapor, (iii) improved error characterization, and (iv) the application of a finer CTM to dynamically convert column retrievals into near-surface mixing ratios. Our PO₃ sensitivity maps surpass traditional FNR-based assessments by quantifying sensitivity magnitudes – factoring in photolysis rates and water vapor – with greater spatial information. Our PO₃ product with its high horizontal coverage will advance our understanding of the drivers of locally-produced ozone pollution, but only at a single snapshot per day. Specifically, our new product provides daily near-clear sky PO₃ and sensitivity maps using bias-corrected OMI (2005-2019, 0.25° × 0.25°) and TROPOMI (2018-2023, 0.1° × 0.1°), with values aligning within 10%. High PO₃ rates (>8 ppbv/hr) appear in urban and biomass-burning regions under strong photochemical activity, including during a heatwave in the northeastern U.S. Photolysis rates are the dominant factor dictating the seasonality of PO₃ magnitudes and sensitivities.

1. Introduction.

To mitigate tropospheric ozone pollution, a pervasive trace gas that impacts human health, climate, and crop productivity (Fleming et al., 2018; Mills et al., 2018; Gaudel et al., 2018), it is essential to quantify the spatiotemporal variations of two primary components: i) the sensitivity of the chemical net production rates of ozone (PO₃) to its two main precursors, nitrogen oxides (NO_x=NO+NO₂) and volatile organic compounds (VOCs), and ii) the magnitude of PO₃ itself. The first component provides insights into the positive and negative contributions of these precursors to PO₃, which are typically categorized as NO_x-sensitive (where PO₃ is influenced mainly by NO_x), VOC-sensitive (where PO₃ is affected primarily by VOCs), and transitional regimes (where PO₃ is responsive to both NO_x and VOCs) (Kleinman et al., 2002; Silman and He, 2002; Duncan et al., 2010). The latter component is crucial for understanding how locally produced ozone, in conjunction with advected or diffused ozone, can lead to high-ozone events (e.g., Kleinman et al., 2002, 2005; Sullivan et al., 2019).

Creating global maps of PO₃ and its sensitivity at spatiotemporal scales relevant to air quality policies is a challenge. Unique instruments can directly measure PO₃ by calculating the difference in ozone molecules from air samples drawn through two distinct tubes – one exposed to sunlight and the other



shielded by an ultra-violet (UV) filter (Cazorla and Brune, 2010; Sadanaga et al., 2017; Sklaveniti et al., 2018). However, these instruments suffer from various interferences, such as heterogeneous chemistry or photo-enhanced loss of ozone within the tubes, and they are limited to sparse super sites that restrict spatial variability. Similarly, box-model simulations of PO_3 , which are observationally constrained by intensive atmospheric composition measurements, are also limited by sparse aircraft sampling (Cazorla et al., 2012; Ren et al., 2013; Mazzuca et al., 2016; Souri et al., 2020a; Schroeder et al., 2020; Brune et al., 2022; Wolfe et al., 2022; Souri et al., 2023a). Currently, our understanding of the global spatiotemporal variability of PO_3 mainly relies on chemical transport models, which can possess significant uncertainties such as those associated with transport, emissions, and dry deposition. Moreover, they may lack the spatial resolution necessary to capture the non-linear dynamics associated with NO_x and thus, ozone chemistry (Valin et al., 2011; Vinken et al., 2011; Yu et al., 2016).

The “gold standard” approach to determine three-dimensional PO_3 within a process-based framework involves running a high-resolution chemical transport model, with prognostic inputs constrained by observations. This approach falls into the realm of an inversion/data assimilation framework (Bocquet et al., 2015). Numerous studies have aimed to constrain various model prognostic inputs, including NO_x and VOCs emissions and/or concentrations, using aircraft and satellite remote sensing retrievals (e.g., Stavrakou et al., 2009, 2016; Souri et al., 2016; Bauwens et al., 2016; Miyazaki et al., 2020; Opacka et al., 2025). Notably, Souri et al. (2020b) developed a non-linear joint inversion of NO_x and VOCs to better constrain PO_3 , thereby shedding light on the impact of recent emission regulations in East Asia on the different chemical pathways governing the formation and loss of surface ozone. However, these studies face a fundamental challenge: discrepancies between simulated fields and observations are often blamed solely on emissions. In fact, such discrepancies can also stem from various model components, including chemical mechanisms, dry deposition, photolysis rates, vertical diffusion, and transport. Given the limited observations available for constraining all of these uncertain parameters, the optimization problem becomes grossly under-determined. This means we lack sufficient information to uniquely determine the optimal values of these parameters altogether. Additionally, the underlying physics of these models is inherently uncertain, necessitating the explicit propagation of model physics errors into our final estimates or the execution of ensemble model realizations to vet the credibility of the top-down estimates across different realizations from a stochastic point of view. Conducting these ensemble optimizations at fine-scale grid boxes around the globe is prohibitively computationally intensive.

At the expense of sacrificing the full capability of a physics-based model, we can take advantage of a statistical approach to predict PO_3 using several observable variables with improved computational efficiency. Chatfield et al. (2010) made an early effort to parameterize the gross production of ozone via $\text{NO}+\text{HO}_2$ through a multivariable power law function that depended on formaldehyde (HCHO), nitrogen dioxide (NO_2), UV photolysis rates, and ambient temperature. Their model successfully reproduced over 60% of the variance observed in the ozone gross production rates. Souri et al. (2023a) introduced a bilinear equation based on $\text{HCHO}\times\text{NO}_2$ and HCHO/NO_2 , which explained more than 80% of the variance in simulated PO_3 . Building on these findings, Souri et al. (2025) developed a regularized piece-wise linear regression to parameterize PO_3 using retrospective aircraft observations and a set of variables, including HCHO/NO_2 , HCHO, NO_2 , $j\text{O}^1\text{D}$ (photolysis frequency for $\text{O}^1\text{D}+h\nu$), and $j\text{NO}_2$ (photolysis frequency for $\text{NO}_2+h\nu$). Their algorithm successfully reproduced over 90% of the variance in observationally-constrained PO_3 with minimal biases across moderately to extremely polluted regions.

These parameterizations present a unique opportunity to globally map PO_3 , as their primary inputs can be largely constrained by well-characterized satellite retrievals with extensive horizontal coverage (Gonzalez Abad et al. 2019). For this reason, Souri et al. (2025), compiled various satellite observations including TROPOspheric Monitoring Instrument (TROPOMI) surface albedo, HCHO, and NO_2 columns in conjunction with pre-computed model fields to populate the inputs to their parametrization, allowing them to generate the first-ever maps of PO_3 worldwide. Because their algorithm had an explicit mathematical form, they were also able to break down PO_3 into HCHO and NO_2 contributions, providing



much more detailed spatial information about ozone sensitivity maps compared to binary information (i.e., NO_x-sensitive or VOC-sensitive) made from HCHO to NO₂ ratios (Martin et al., 2004; Duncan et al., 2010; Choi et al., 2012; Choi and Souri, 2015a, b; Jin et al., 2017; Schroeder et al., 2017; Souri et al., 2017; Jeon et al., 2018; Tao et al., 2022; Jonhson et al., 2024). However, HCHO to NO₂ ratios (known as formaldehyde to nitrogen dioxide ratios – FNR) were a central component of their algorithm to transform the non-linear ozone chemistry into several linear segments (i.e., a piecewise regression).

The inclusion of FNR in Souri et al. (2025) might introduce several complications, such as i) the amplification of unresolved systematic and random errors in satellite retrievals associated with PO₃ estimates, and ii) discounting the dependency of PO₃ sensitivity to HCHO and NO₂ concentrations as function of available light and water vapor. In fact, FNR does not provide useful information about ozone chemistry in less photochemically active environments, such as early morning or late afternoon conditions (known as light-limited or radical-limited conditions). Although the parametrization of PO₃ crafted in Souri et al. (2025) relied on photolysis rates, the sensitivity of PO₃ to NO₂ (a proxy for reactive nitrogen) and HCHO (a proxy for VOC reactivity) did not directly depend on photolysis rates. Therefore, the present work aims to enhance the capability of the algorithm designed in Souri et al. (2025) using a machine learning approach that can effectively establish a robust non-linear relationship between PO₃ and various observable geophysical variables without the need for segregation or linearization based on concentrations of ozone precursors, light intensity, or humidity.

The new product of PO₃ along with spatially varying ozone sensitivity maps using bias-corrected OMI and TROPOMI retrievals are generated globally for 2005-2023. We will document the advantages of this algorithm over the older one and how the new results can bring fresh insights into PO₃ behavior across various seasons, locations, and anomalous events (e.g., heatwaves).

2. Data

2.1. Satellite Retrievals

2.1.1. TROPOMI HCHO and NO₂

We use daily level-2 (L2) products of TROPOMI (v2.4-v2.5) tropospheric NO₂ and total HCHO columns (v2.4-v2.6) obtained from UV-Vis radiances (~328-496 nm) onboard the European Space Agency's (ESA's) Sentinel Precursor (S5P) spacecraft with an equatorial overpass time of ~1330 local standard time (LST) (Veefkind et al., 2012; van Geffen et al. 2022; De Smedt et al. 2021). These products offer near-daily global coverage of NO₂ and HCHO columns at a horizontal resolution of 7.2 km (reduced to 5.6 km after August 2019) by 3.6 km at nadir, extending to approximately 14 km at the edges of the scanline, with a swath width of 2600 km. The data products used in this study span from May 2018 to the end of 2024. The retrieval process follows a two-step framework: first, a differential spectral fitting algorithm is used to determine the number of integrated molecules along the slant light path, and second, air mass factor calculations are done based on simulated gas absorber profiles and radiative transfer model calculations to convert slant columns into vertical ones.

Both products have been thoroughly vetted against ground-based remote sensing retrievals, including the multi-axis differential optical absorption spectrometer (MAX-DOAS) (De Smedt et al., 2021; Verhoelst et al., 2021; van Geffen; Souri et al., 2025) and Fourier transform infrared spectroscopy (FTIR) (Vigouroux et al., 2020; Souri et al., 2025), showing a general tendency towards underestimation in polluted regions. We include in our study only pixels with a quality flag (*q_value*) exceeding 0.5 and 0.75 for HCHO and NO₂ products, respectively. The quality flag encapsulates errors coming from clouds, snow, surface refractivity, and algorithm performance. The selected values are based on the user manual recommendation (Eskes et al., 2020; De Smedt et al., 2021). Additionally, we bias correct the columns using the offset (additive term) and slope (multiplicative term) determined from a global comparison of MAX-DOAS/FTIR



and these datasets, as described by Sourì et al. (2025). The resulting daily bias-corrected HCHO and NO₂ columns, along with the retrieval errors, are mapped onto a 0.1°×0.1° global grid using a mass-conserved bilinear interpolation approach described in Sourì et al. (2024).

2.1.2. OMI HCHO and NO₂

We use the Quality Assurance for the Essential Climate Variables (QA4ECV) NO₂ daily Level 2 product (Boersma et al., 2018) which is based on global radiances captured by the Ozone Monitoring Instrument (OMI) sensor aboard NASA's Aura spacecraft. This product is retrieved with a similar overpass time as TROPOMI. The horizontal resolution of the product ranges from 13×24 km² at nadir to 165×13 km² at the edge of the scanline. It relies on OMI Collection 3 radiance data. Since 2008, OMI has faced significant anomalies resulting in the loss of reliable data in areas of its detectors, a situation referred to as the "row anomaly." This has led to inconsistent spatial resolution and global coverage throughout its operational phase. However, the unaffected detectors have demonstrated a high level of stability over the past two decades, making this product suitable for long-term trend analysis. Detailed description of the retrieval algorithm, along with validation against ground remote sensing data, can be found in Boersma et al. (2018), Compernelle et al. (2020), and Pinardi et al. (2020). We include good quality pixels based on an effective cloud fraction below 50%, a quality processing flag parameter equal to zero, and exclusion of snowy regions. Additionally, we discard the last two rows of the detector because of their poor horizontal resolution. We use the OMI NO₂ product for the period from 2005 until the end of 2019. To correct for offset and slope in this product, we apply the statistics from Pinardi et al. (2020), who compared this product against MAX-DOAS observations, factoring in an empirical dilution adjustment to address the mismatch between the OMI resolution and MAX-DOAS.

We also use the OMI Smithsonian astrophysical observatory (SAO) daily HCHO Level 2 product from the same sensor, which is generated using a newly developed algorithm and Collection 4 OMI radiances (Ayazpour et al. 2025; Nowlan et al., 2023). This improved algorithm enhances the radiance information content used to retrieved HCHO columns, significantly reducing noise in the slant column fit. The stability of this product in extracting new information related to long-term global trends of HCHO has been well demonstrated in recent studies (Sourì et al., 2024; Anderson et al., 2024). Ayazpour et al. (2025) validated the product against the global FTIR network and found that the HCHO columns tend to be biased low in polluted regions. Accordingly, we use their statistics to adjust for both offset and slope associated with the data. We include only good data following the quality flag provided with the dataset along with effective cloud fraction below 40%. Both bias-corrected OMI products are mapped onto a global grid with a resolution of 0.25°×0.25° using the same algorithm used for TROPOMI.

2.1.3. Surface albedo

To estimate near-surface photolysis rates of jO¹D (O₃+hν, <350 nm) and jNO₂ (NO₂+hν, ~400-500 nm) used in the parametrization of PO₃, we are required to provide reasonable surface albedo estimates (Section 2.4). We use a monthly Directionally Dependent Lambertian-Equivalent reflectivity (DLER) climatology derived from TROPOMI radiances at the spatial resolution of 0.125°×0.125°; the product is in good agreement with the MODIS BRDF product (Tilstra et al., 2024). This climatology has two sets of values for both shortwave (328 nm) and longwave UV (463 nm) that are used separately for calculating jO¹D and jNO₂, respectively. We use only the isotropic part of the DLER product (named *minimum_LER*), which is added to an offset coefficient provided with the dataset.

2.2. Aircraft Measurements

The use of aircraft observations is twofold: first, they provide a vast number of measured geophysical variables suitable to simulate our observationally-constrained PO₃ training dataset (Section 3.1); second, they enable a rigorous validation of column-to-PBL conversion factors derived from a chemical transport model (Appendix B). We use the dataset compiled by Sourì et al. (2025), who curated



various aircraft campaigns measuring photolysis rates, meteorological variables, and atmospheric composition from varying atmospheric conditions, including urban/suburban settings (DISCOVER-AQs, and KORUS-AQ), high-vegetated regions (SENEX), and remote areas (INTEX-B and AToms). The sampling frequency varies from 10-sec to 30-sec. More detailed information regarding the choice of instrument, gap filling, and data exclusion can be found in Souri et al. (2025).

2.3. *MINDS simulations*

We use a global chemical transport model simulation designed to support trace gas retrievals. The simulation, called Multi-Decadal Nitrogen Dioxide and Derived Products from Satellites (MINDS), was generated using the Goddard Earth Observing System (GEOS) Earth system model (Molod et al., 2015; Nielsen et al., 2017) equipped with the full chemistry Global Modeling Initiative (GMI) mechanism (Duncan et al., 2007; Strahan et al., 2007) and coupled with the Goddard Chemistry Aerosol Radiation and Transport (GOCART) aerosol module (Chin et al., 2002). The rapid radiative transfer model, which was designed for global climate models (GCMs) and is known as the Radiative Transfer Module for GCM (RRTMG), calculates the longwave and shortwave radiation influenced by aerosols simulated by GOCART, enabling the incorporation of the direct effects of aerosols on meteorological conditions (Nielsen et al., 2017). The model is setup at c360 grid ($0.25^\circ \times 0.25^\circ$) and covers the period of 1993 until the end of 2023. The model follows 72 hybrid sigma values ranging from the surface to 0.01 hPa. Several prognostics inputs related to meteorology, including water vapor, are constrained by MERRA-2 reanalysis (Orbe et al., 2017). Lightning production of NO is parametrized based on the simulated convection. The model uses the Monitoring Atmospheric Chemistry and Climate and CityZen (MACCity) inventory (Granier et al., 2011) of anthropogenic emissions downscaled to $0.1^\circ \times 0.1^\circ$ using the Emissions Database for Global Atmospheric Research version 4.2 (EDGAR 4.2). These anthropogenic emissions change by year and month. Biomass burning emissions rely on the Fire Energetics and Emissions Research (FEER) dataset (Ichoku and Ellison, 2014). Biogenic emissions are modeled by the Model of Emissions of Gases and Aerosols from Nature (MEGAN) v2.1 (Guenther et al. 2012). It is known that isoprene emissions in MEGANv2.1 are largely overestimated (Bauwens et al., 2016; Souri et al., 2020b), therefore they are scaled down by a factor of two.

2.4. *TUV NCAR Photolysis Rates Look-up Table*

To estimate jNO_2 and jO^1D , we refer to a detailed look-up table provided by the Framework for 0-D Atmospheric Modeling (F0AM) model (Wolfe et al. 2016). This table is developed for clear-sky conditions based on over 20,064 solar spectra calculations. The data encompasses a broad spectrum of solar zenith angles (SZA) from 0° to 90° in 5° increments, altitudes ranging from 0 to 15 km in 1 km steps, overhead total ozone columns from 100 to 600 DU in increments of 50 DU, and surface UV albedo values from 0 to 1 in 0.2 increments. These calculations were carried out using NCAR's Tropospheric Ultraviolet and Visible radiation model (TUV v5.2), along with cross sections and quantum yields from IUPAC and JPL (Wolfe et al., 2016). Information on SZA and surface elevation is obtained from the L2 TROPOMI/OMI granule data. Surface albedo is based on the TROPOMI DLER climatology (Section 2.1.3). The overhead total ozone columns are derived from MINDS simulations (Section 2.3). For any values that fall between the entries in the tables, we apply a linear interpolation method.

2.5. *Empirical PO_3 estimates using LASSO*

We will compare our new product (Section 3.2) to an empirical method developed by Souri et al. (2025), who took advantage of simulated PO_3 data constrained by aircraft measurements to parameterize PO_3 using four geophysical variables: NO_2 , HCHO , jNO_2 , and jO^1D . Their algorithm used a piecewise L1-regularized linear regression model known as Least Absolute Shrinkage and Selection Operator (LASSO). Since the algorithm was based on a linear model which was ill-suited for the non-linear ozone chemistry, it was necessary to linearize the parameterization using various thresholds for FNRs. Despite the method's simplicity, Souri et al. (2025) were able to reproduce approximately 88% of the variance with low biases (less than 20%) in observationally-constrained PO_3 . Using the empirical method, they generated the first



230 maps of PO_3 by combining bias-corrected TROPOMI HCHO and NO_2 columns, simulated photolysis rates,
231 and a global transport model designed for the conversion from column measurements to the planetary
232 boundary layer (PBL).

233 To isolate the performance of the PO_3 estimator used in Souri et al. (2025) as compared to the
234 proposed algorithm in this study, we will ensure that the input variables, including the mixing ratios of
235 HCHO and NO_2 within the PBL as well as the photolysis rates, remain identical for both the empirical
236 product and our new algorithm. Henceforth, we will refer to this empirical product as “ PO_3 LASSO”.

237 3. Methodology

238 Figure 1 illustrates the three-stage process of our newly developed algorithm to operationally
239 produce long-term maps of PO_3 within the PBL along with the sensitivity and error maps. The product is
240 called “ PO_3 DNN”.

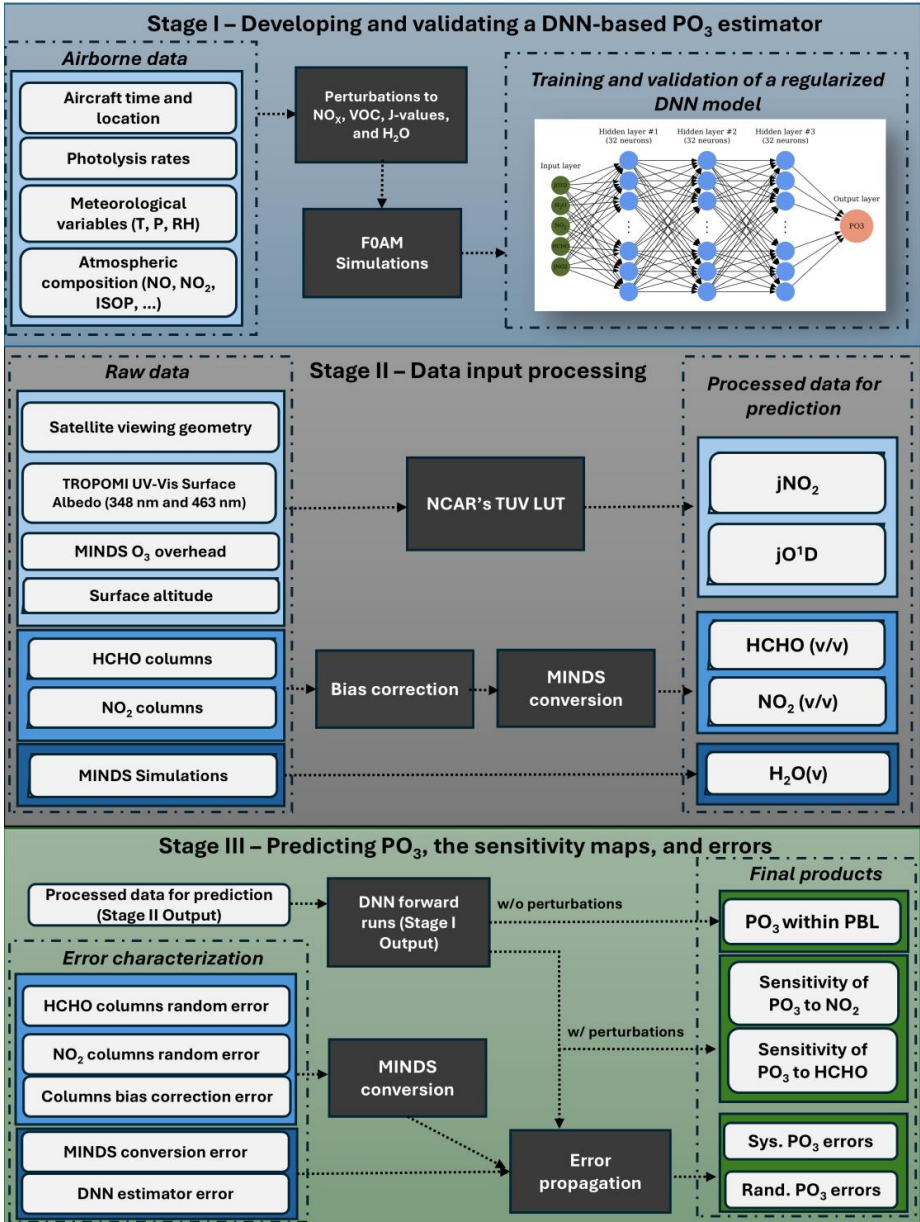
241 *Stage I* – This stage serves as the foundation for the product, focusing on parameterizing PO_3 using
242 a regularized Deep Neural Network (DNN). The training dataset, detailed in Section 3.1, is derived from
243 an observationally-constrained F0AM box model that provides simulated PO_3 along with various
244 atmospheric quantities directly or indirectly constrained by aircraft measurements. The decision to make
245 use of aircraft data is based on two main factors: i) they capture real-world atmospheric conditions across
246 diverse parts of the atmosphere and various geographic regions, and ii) the significant fluctuations inherent
247 in the data rigorously test the DNN’s capability to generalize (i.e., to fit the model through the data rather
248 than merely to the data). However, a notable limitation of aircraft data is its restriction to specific
249 atmospheric conditions. To address this, we have expanded the training dataset by perturbing the inputs to
250 the F0AM model (Section 3.1), resulting in a synthetic dataset. This expanded training dataset is then used
251 for validation, testing, and calibration of the DNN algorithm.

252 *Stage II* – The objective of this stage is to prepare spatiotemporal geophysical variables necessary
253 for the prediction of PO_3 (done in Stage III). We need five parameters on a global scale with daily frequency:
254 $j\text{NO}_2$, $j\text{O}^1\text{D}$, HCHO, NO_2 , and $\text{H}_2\text{O}(\text{v})$. To generate global daily maps of near-surface photolysis rates, we
255 use the NCAR’s look-up table as detailed in Section 2.4; this table relies on SZA, which varies with time
256 and location, as well as surface UV-Vis albedo, ozone overhead columns, and surface altitudes. Data on
257 both SZA and surface altitude are acquired from the satellite L2 products. Ozone overhead columns are
258 from MINDS. For surface UV-Vis albedo, we use two different wavelengths based on TROPOMI’s
259 climatology (Section 2.1.3). These calculations assume clear sky conditions, which are somewhat achieved
260 by the effective cloud fraction thresholds derived from both the OMI and TROPOMI products. However,
261 the presence of partially cloudy pixels and aerosols can introduce uncertainties in calculated photolysis
262 rates. To address these effects using a radiative transfer model (e.g., RRTMG), long-term observations of
263 three-dimensional optical properties of clouds and aerosols on a global scale are needed. Unfortunately,
264 such records are typically limited to narrow paths of spaceborne lidar observations, which carry
265 considerable uncertainties (Thorsen and Fu, 2015). Assuming that both clouds and aerosols attenuate UV-
266 Vis sunlight down to the surface—creating a shielding effect rather than a brightening effect—over bright
267 urban areas, the omission of aerosols and clouds in our product is likely to result in an overestimation of
268 near-surface photolysis rates over those areas. Our algorithm uses HCHO and NO_2 columns obtained from
269 OMI or TROPOMI, which are bias-corrected against ground remote sensing data. These measurements are
270 then transformed into the mixing ratios in the PBL region using the vertical distribution of HCHO and NO_2
271 profiles simulated by MINDS. The final variable is the average number of water vapor ($\text{H}_2\text{O}(\text{v})$) molecules
272 per cubic meters in the PBL region at the satellite overpass time, which is obtained directly from the MINDS
273 simulation. It is important to note that the MINDS simulation is based on constraints from MERRA-2
274 reanalysis, underscoring that the $\text{H}_2\text{O}(\text{v})$ simulations are constrained by observations.



275 *Stage III* – In the final stage, we predict PO_3 , generate sensitivity maps, and provide both systematic
276 and random errors associated with these estimates. To create PO_3 maps, we input the five parameters from
277 Stage II into the DNN model developed in Stage I. To generate the sensitivity maps of PO_3 in relation to
278 NO_2 and HCHO, we apply perturbations to NO_2 and HCHO based on the methodology described in Section
279 3.3. These perturbations also serve another purpose which is to propagate the errors associated with the
280 retrievals of HCHO and NO_2 , as well as their corresponding conversion factors from MINDS into the final
281 product. A comprehensive explanation of the error budget and characterization can be found in Section 3.4.

282 While we perform Stage I only once to establish a PO_3 estimator, we need to run Stage II and III
283 for any desired location/time or spatial resolution. The need to operationally run these two stages has
284 motivated us to create an open-source and object-oriented Python package called *ozonerates* v1.0 (Souri
285 and Gonzalez Abad, 2025), which is capable of running all steps while leveraging parallel computation.



286

287 **Figure 1.** Processing stages developed to operationally generate PO₃ and sensitivity maps along with daily
288 frequency errors on a global scale. Stage I aims to establish a regularized DNN model based on synthetic
289 and real-world aircraft measurements. Stage II prepares the necessary satellite-based input features used for
290 PO₃ prediction in Stage III. Stage III feeds the DNN model with Stage II values and some statistical error
291 analysis to populate the final product.



292 3.1. Training dataset generation using F0AM box model

293 To establish a relationship between several geophysical variables related to PO_3 , we use F0AM
 294 version 4 box model (Wolfe et al., 2016). This model is capable of simulating detailed chemical kinetics
 295 based on user inputs regarding meteorological variables, atmospheric compositions, and photolysis rates.
 296 F0AM uses a solver for ordinary differential equations (ODEs) designed for stiff systems, which allows it
 297 to determine the chemical evolution of all species included in the selected chemical mechanism. We adhere
 298 to previous configurations that apply the Carbon Bond 6 (CB06, r2) chemical mechanism within F0AM
 299 (Souri et al., 2020a; Souri et al., 2023a; Souri et al., 2025). The model is constrained by data collected
 300 during aircraft campaigns, including meteorological data, photolysis rates, and various trace gas
 301 concentrations. Additional details regarding the selection of instruments, bias corrections for photolysis,
 302 choices of dilution factors, and other configurations can be found in Souri et al. (2025). We incorporate data
 303 from seven aircraft campaigns, including DISCOVER-AQ (Texas, Washington, Colorado), KORUS-AQ,
 304 ATOMs, INTEX-B, and SENEX, to further constrain the model. Souri et al. (2025) demonstrated that this
 305 setup effectively reproduces several unconstrained yet measured compounds, such as HCHO, HO_2 , OH,
 306 and PAN; moreover, the performance of the model was on par with other studies (e.g., Brune et al., 2020;
 307 Brune et al., 2022; Miller and Brune, 2022), indicating that it is a suitable model setup for understanding
 308 local ozone chemistry. This model-derived dataset consists of $\sim 134\text{k}$ points.

309 A limitation to the training dataset prepared by Souri et al. (2025) originates from the fact that only
 310 a subset of atmospheric conditions could be observed by the suborbital missions. A remedy for this
 311 limitation is to synthetically regenerate data by systematically perturbing several of the inputs used in the
 312 F0AM model. As a result, we apply a scaling factor, ranging from 0.1 up to 10 in 12 evenly-spaced steps,
 313 separately to NO_x , VOCs, $\text{H}_2\text{O}(\text{v})$, and photolysis rates. This expands the dataset to ~ 6.4 million datapoints,
 314 covering a much wider range of atmospheric states. Once the simulations are done, we determine simulated
 315 PO_3 by:

$$316 \quad \text{PO}_3 = \text{FO}_3 - \text{LO}_3 \quad (1)$$

317 where LO_3 is all possible chemical loss pathways of ozone (negative stoichiometric multiplier matrix) and
 318 FO_3 is all possible chemical pathways producing ozone molecules (positive stoichiometric multiplier
 319 matrix). This equation is also known as ozone tendency.

319 3.2. DNN architecture and configuration

320 The overall architecture of the DNN model is portrayed in Figure 2. The design consists of three
 321 fully-connected hidden layers each having 32 neurons. The neurons are equipped with rectified linear unit
 322 (ReLU) activation functions. The training dataset (~ 6.4 millions) is split into 20% test, 24% validation, and
 323 56% training. Training inputs to the parametrization consists of HCHO, NO_2 , jO^1D , jNO_2 , and $\text{H}_2\text{O}(\text{v})$.
 324 Prior to the training, we normalize them, such that each feature (x) is rescaled according to $x' = \frac{x - \mu}{\sigma} x$,
 325 where μ and σ represent the mean and standard deviation of the feature, respectively, ensuring a mean of
 326 zero and a variance of one. The optimization (training) of the DNN follows the backpropagation rule armed
 327 with Adaptive Moment Estimation (ADAM) optimizer which is known to perform well with noisy data
 328 (Kingma and Ba, 2014). The initial learning rate is set to 10^{-5} . We use 500 epochs. The loss function (L) of
 329 the optimization problem is:

$$330 \quad L = \frac{1}{2} \sum_{k=1}^N (y_k - o_k)^2 + \lambda \sum_{i=1}^p w_i^2 \quad (2)$$

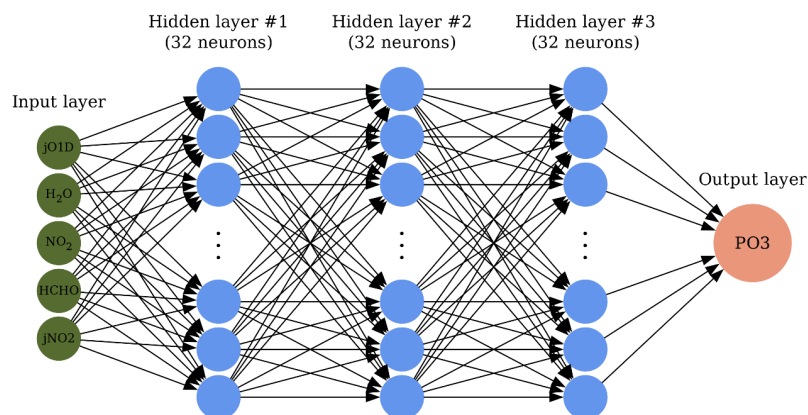
331 where the first term on the right side represents the mean squares error (MSE) of the prediction derived
 from difference between the target PO_3 (y) and the predicted PO_3 (o). N represents the number of training



332 datapoints. The second term is L2-regularization with a factor of λ to reduce the squares of p number of
333 neuron weights (w).

334 An important aspect of this optimization is the use of L2 regularization, which effectively helped
335 us determine the optimal number of hidden layers and neurons. L2 regularization penalizes the cost function
336 if an illusion of high prediction accuracy (the first term) is achieved with excessive variance in the solution
337 (weights). Failing to balance the prediction error and the solution variance can lead to overfitting, which
338 harms model performance in two ways: i) it results in erroneous predictions for atmospheric conditions that
339 fall outside the training dataset; ii) it diminishes the physical interpretability of the statistical model because
340 of large fluctuations in the weights, a common issue in regression models known as collinearity. When we
341 used too many neurons or layers, the regularization penalized the weights, causing a substantial proportion
342 to approach zero (not shown), indicating that those neurons were unnecessary. However, incorporating
343 regularization does have some drawbacks: i) it requires a smaller initial learning rate (set to 10^{-5}) to avoid
344 falling into local minima, which demands more computational resources; and ii) the regularization factor
345 also needs to be optimized. We found that a value of $\lambda = 10^{-5}$ provided the best results among the set of
346 values [10^{-4} , 10^{-5} , and 10^{-6}], based on the symmetry in the statistical distributions of the test residuals, MSE,
347 and the overall level of physical interpretability observed in the sensitivity tests.

348 The implementation of the DNN model is done using the open-source *TensorFlow* application
349 programming interface (API) package in *Python* (Abadi et al., 2016). To thoroughly validate the
350 performance of this model from various angles we i) compare the DNN prediction with the test data using
351 various standard metrics, ii) investigate the evolution of the loss function derived from both the training set
352 and the validation one over epochs, iii) study the physical explanation of the response of PO_3 to NO_2 and
353 HCHO , water vapor, and photolysis rates, and iv) finally compare the DNN results to PO_3 LASSO. We will
354 use a number of statistical metrics, including the coefficient of the determination (R^2), mean bias, mean
355 square error, mean absolute error, and root mean square error (RMSE), to carry out the quantitative
356 assessment (Section 4.1).



357
358 **Figure 2.** The architecture of the DNN model. The model contains three hidden layers with 32 neurons
359 each.

360 3.3. Sensitivity calculations

361 To elucidate the response of PO_3 to its inputs, we calculate the semi-normalized sensitivities
362 through the finite difference method:

$$SP03_i = \frac{[PO3]_i^{110\%} - [PO3]_i^{90\%}}{0.2} \quad (3)$$



where $[PO_3]_i^{110\%}$ and $[PO_3]_i^{90\%}$ are PO_3 from perturbing input parameters ($i=1$ for NO_2 , and $i=2$ for $HCHO$) by 1.1 and 0.9 scaling factors. A mathematical proof showing that these sensitivity calculations are equivalent to the directional derivative is provided in Appendix A.

3.4. Error budget and characterization

Since the PO_3 DNN integrates atmospheric models, satellite trace gas retrievals, ground remote sensing, and a machine learning approach, it contains various sources of errors, some of which will be formulated in this section. Spatially and temporally averaging satellite-based products is a common practice to reduce noise and fill gaps; therefore, we attempt to separate systematic errors (irreducible by averaging) from random ones (reducible by averaging). We assign the total PO_3 within PBL region error (e_{total}) based on the following equation:

$$e_{total} = \sqrt{e_{syst}^2 + e_{rand}^2} \quad (4)$$

where e_{syst} and e_{rand} are systematic and random errors associated with PO_3 estimates. Systematic errors account for the errors associated with the bias correction of OMI and TROPOMI against ground remote sensing retrievals ($e_{HCHO_bias_c}$ and $e_{NO_2_bias_c}$), the model-based conversion of columns to the PBL mixing ratios ($e_{HCHO_conversion}$, $e_{NO_2_conversion}$), and the DNN estimator error (e_{DNN}), and are given by:

$$e_{syst} = \sqrt{e_{HCHO_bias_c}^2 + e_{NO_2_bias_c}^2 + e_{HCHO_conversion}^2 + e_{NO_2_conversion}^2 + e_{DNN}^2} \quad (5)$$

$$e_{HCHO_bias_c}^2 = \left(\frac{\partial PO_3}{\partial HCHO} \cdot \gamma \cdot e_{bc-HCHO} \right)^2 \quad (6)$$

$$e_{NO_2_bias_c}^2 = \left(\frac{\partial PO_3}{\partial NO_2} \cdot \gamma \cdot e_{bc-NO_2} \right)^2 \quad (7)$$

$$e_{HCHO_conversion}^2 = \left(\frac{\partial PO_3}{\partial HCHO} \cdot VCD_{HCHO} \cdot e_{conv-HCHO} \right)^2 \quad (8)$$

$$e_{NO_2_conversion}^2 = \left(\frac{\partial PO_3}{\partial NO_2} \cdot VCD_{NO_2} \cdot e_{conv-NO_2} \right)^2 \quad (9)$$

where γ is the conversion factor of the satellite total to the PBL columns translation based on MINDS and the formulation by Sourì et al. (2025); $e_{bc-HCHO}$ and e_{bc-NO_2} in column units, are calculated following the formulation from Sourì et al. (2025) who used the errors of slope and offset obtained from the comparison of satellite VCDs to ground remote sensing benchmarks; $e_{conv-HCHO}$ and $e_{conv-NO_2}$ are quantified by validating the simulated conversion factors compared to those of aircraft vertical spirals (Appendix B). The unit for these two errors is ppbv per the column unit; accordingly, we multiply these terms to satellite VCDs. The last term in Eq.5 is a fixed systematic error associated with the DNN estimates which will be quantified based on the MSE of the DNN prediction. Both $\frac{\partial PO_3}{\partial HCHO}$ and $\frac{\partial PO_3}{\partial NO_2}$ are derived from the sensitivity calculations from Eq.3 divided by the satellite columns. All error terms in Eqs.6-9 are spatially and temporally invariant, but the derivatives vary from pixel to pixel resulting in spatiotemporally-varying systematic errors.

Random errors originate from the uncertainty estimates coming with the TROPOMI and OMI L2 products and are somewhat reducible by averaging, and are given by:

$$e_{rand} = \sqrt{\left(\frac{\partial PO_3}{\partial HCHO} \cdot \gamma \cdot e_{rand-HCHO} \right)^2 + \left(\frac{\partial PO_3}{\partial NO_2} \cdot \gamma \cdot e_{rand-NO_2} \right)^2} \quad (10)$$

where $e_{rand-HCHO}$ and $e_{rand-NO_2}$ are random retrieval errors. All terms in Eq.10 vary by time and location.

Table 1 summarizes the numbers used in the above equations and their origin.

396 **Table 1.** Values used in error calculations.

Error terms	Systematic/Random	Value	Unit	Source
e_{bc-NO_2} and $e_{bc-HCHO}$	Systematic	$0.01 \times VCD + 0.06$	$\times 10^{15}$ molec./cm ²	Souri et al. (2025)
$e_{conv-HCHO}$ and $e_{conv-NO_2}$	Systematic	0.09	ppbv/(10^{15} molec./cm ²)	Appendix B
e_{DNN}	Systematic	0.78	ppbv/hr	Section 4.1
$e_{rand-NO_2}$ and $e_{rand-HCHO}$	Random	Variable	$\times 10^{15}$ molec./cm ²	L2 Products

397

398 It is important to acknowledge that the defined total error budget here is only a good guess and
 399 optimistic. Some underlying sources of error, which are difficult to quantify, are not included. For example,
 400 errors related to the training dataset derived from the F0AM model are challenging to assess because of the
 401 lack of PO₃ measurements. We assume other inputs to the PO₃ parametrization, such as surface albedo and
 402 H₂O(v), to be error-free. Additionally, all datasets used to estimate PO₃ contain spatial representation errors
 403 (Souri et al. 2023), which are difficult to measure without knowing their true state of global spatial
 404 variability. There are also assumptions regarding the equations mentioned earlier. For instance, it is assumed
 405 that the validation of conversion factors can account for all systematic issues related to the vertical
 406 distribution of NO₂ and HCHO in MINDS. Furthermore, we presume that the reported retrieval errors are
 407 mostly random; however, this is not the case (Eskes et al., 2003; Boersma et al. 2018), and distinguishing
 408 between these errors is not straightforward.

409 In case of oversampling of the PO₃ product both temporally and spatially, the total error will be given by:

$$e_{total} = \sqrt{\frac{1}{m} \sum e_{syst}^2 + \frac{1}{m^2} \sum e_{rand}^2} \quad (11)$$

410 where m is the total number of samples. Eq.11 suggests that the systematic errors are persistent across all
 411 samples and are not reducible by averaging, whereas the random errors become smaller by root square of
 412 samples. In this equation, the assumption is that the root-mean-square of the systematic errors is a good
 413 approximation of the systematic errors in the oversampled data because they are independent of each other.

414 4. Results and Discussion

415 In this section, we begin by validating and contrasting PO₃DNN against PO₃LASSO. Following
 416 that, we use OMI to investigate the spatiotemporal variability of PO₃ and its sensitivity to photolysis rates,
 417 HCHO, and NO₂ globally. We provide an application of the data to understand the effect of an extreme heat
 418 wave on PO₃. Afterward, we offer a comprehensive global view of the PO₃ estimates algorithm by
 419 integrating data from the TROPOMI compared with that one based on OMI. Finally, we document the total
 420 error budget of the products.

421 4.1. DNN performance

422 We investigate the predictive power of the DNN algorithm against both validation and test data for
 423 each air quality campaign or the entire aircraft dataset (Section 2.2). Figure 3 demonstrates the learning
 424 curves (i.e., the evolution of MSE of prediction against the number of epochs corresponding to the number
 425 of iterations of training the network for one cycle). All training datasets described in Section 3.1 are used
 426 in this stage. Except for the early stages of training, both training and validation curves closely follow each
 427 other, indicating that we possibly do not have overfitting issues. The curves are fairly smooth, resulting



from using the ADAM optimizer with a strictly small learning rate initially. Both curves converge to MSE below 0.8 ppbv/hr which we use to assign the error of PO₃DNN prediction in Eq.5.

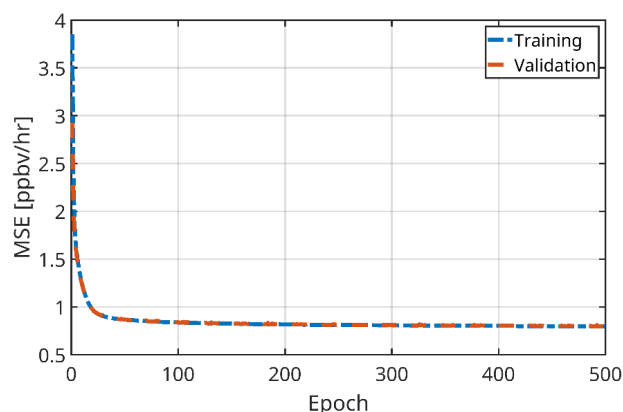
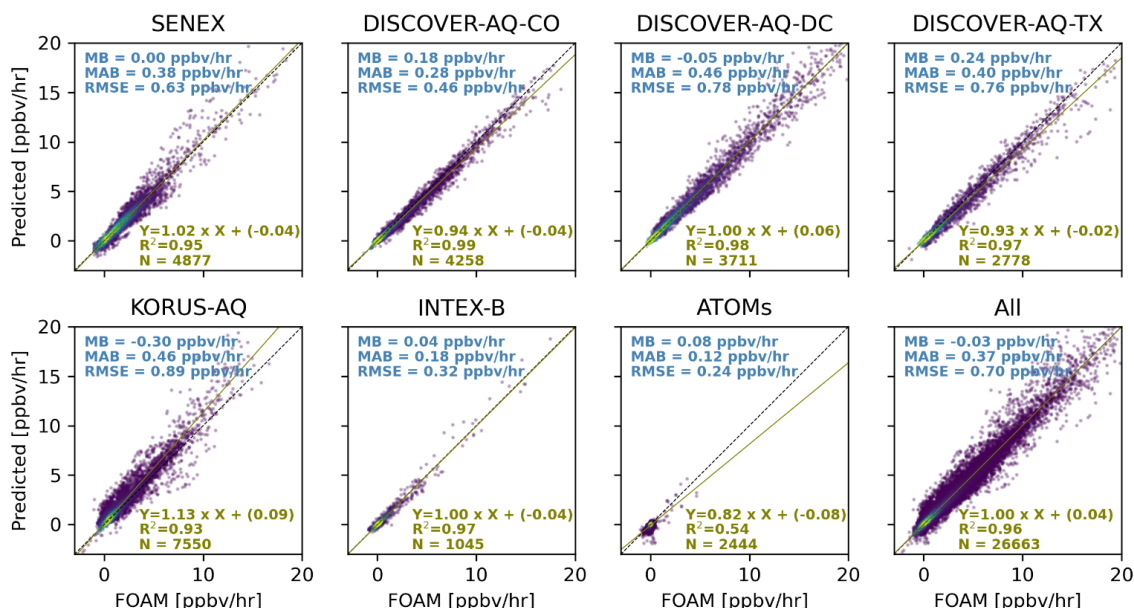


Figure 3. The learning curve shows the evolution of training and validation MSEs as a function of epochs.

PO₃DNN has promising skill at predicting PO₃ across various atmospheric conditions. Figure 4 presents a comparison of the predicted PO₃ values against observationally-constrained F0AM values for the test data for each suborbital mission. A similar comparison, which includes all data points measured during each mission, can be found in Figure S1. The primary reason for highlighting the test data is that they have never been used to fine-tune the DNN parameters. There is a strong correlation between the predictions and the benchmarks across most campaigns for both the test data points (Figure 4) and the complete set of aircraft measurements (Figure S1). Notably, the slope for the "All" test dataset is close to the unity line. The DNN algorithm can reproduce over 96% of the variance in the test data. The model performs significantly better than PO₃LASSO over INTEx-B compared to LASSO (as shown in Figure 7 in Sourì et al., 2025). While the DNN's performance over the ATom campaigns is less impressive than in other areas, it still represents a considerable improvement over LASSO, which was unable to reproduce PO₃ in pristine regions ($R^2 < 0.05$). One key factor contributing to this improvement is the inclusion of H₂O(v) in the input. Various parameters, including HO_x, are known to influence PO₃ in remote regions, but these factors were not included in our parametrization. The method does not artificially inflate results by introducing non-physical relationships in remote regions; the inability of the DNN to fully explain PO₃ during AToms suggests that it does not force unrealistic relationships between PO₃ and the inputs to completely align with the F0AM results, leaving areas for future improvement in parametrization over remote regions.



451

452 **Figure 4.** Scatterplots comparing observationally-constrained FOAM model PO_3 and the predictions that
 453 were based on the DNN for the test data from each air quality campaign. The test data have never been used
 454 for hyper tuning the algorithm. “All” denotes all test data.

455 4.2. Advantages of PO_3 DNN over PO_3 LASSO

456 There are primarily four major benefits of PO_3 DNN over PO_3 LASSO that make the former parameterization
 457 a superior algorithm. The discussion of these advantages is as follows:

458 — *Higher predictive power:* PO_3 LASSO predicted PO_3 for all datapoints collected from the suborbital
 459 missions with a $R^2=0.88$, $RMSE=1.2$ ppbv/hr, and a slope of 0.87 (Souri et al., 2025), whereas PO_3 DNN
 460 reproduced the exact datapoints (Figure S1) with a $R^2=0.96$, $RMSE=0.7$ ppbv/hr, and a slope of 1.00.
 461 Furthermore, as shown in Figure 4, PO_3 DNN has a great degree of generalization for datapoints outside
 462 of the training/validation data points. Consequently, these statistics suggest that DNN is a more
 463 powerful predictor.

464 — *Better representation of PO_3 over remote regions:* One notable limitation of PO_3 LASSO was its
 465 inadequate representation of PO_3 in remote regions, such as during the ATOMs or INTEx-B campaigns.
 466 This led Souri et al. (2025) to entirely mask PO_3 estimates below 1 ppbv/hr. In these remote areas, PO_3
 467 is typically influenced by the reactions between ozone and HO_x in addition to jO^1D and H_2O . While
 468 Souri et al. (2025) attempted to incorporate H_2O into the LASSO parameterization, the algorithm
 469 assigned a zero coefficient to this parameter because of the use of the L1-regularization term. This term
 470 typically assigns a zero coefficient for a geophysical variable that is either irrelevant to the target or
 471 shows strong non-linear relationship with the target. PO_3 LASSO did not factor in $H_2O(v)$ because
 472 $H_2O(v)$ exhibits a non-linear relationship with PO_3 – although the reaction between O^1D and H_2O can
 473 suppress ozone formation through the removal of O^1D , it produces two molecules of OH regenerating
 474 ozone in polluted places (Bates and Jacob, 2019). Consequently, the non-linear relationship between
 475 H_2O and PO_3 is one that LASSO was unable to capture. While we could have addressed this by dividing
 476 the training dataset into different humidity levels (i.e., dry and humid), such an approach would have
 477 resulted in more discretization in the parametrization. Conversely, PO_3 DNN can consider the non-linear



relationship between H_2O and PO_3 without the need for empirical linearization. We observe a significant improvement in predicted PO_3 for both AToms and INTEX-B campaigns compared to Souri et al. (2025).

— *Diminished satellite error effects:* The reliance of PO_3 LASSO on FNR increases the contamination of PO_3 predictions from satellite random noise. This primarily occurs because satellite errors associated with HCHO and NO_2 adversely influence FNR (see Figure 12 in Souri et al. (2023a)), resulting in noise in the empirical linearization approach used in PO_3 LASSO. Even if we assume that all inputs to the PO_3 LASSO parameterization, except for FNR, are error-free, the inherent randomness from choosing among four different sets of equations segregated by the noisy FNR will still feed noise into the final estimate. Although PO_3 DNN is inevitably influenced by satellite errors because of its dependence on HCHO and NO_2 columns, it does not exacerbate these errors because it operates independently of FNR. To demonstrate this tendency, Figure 5 shows the global PO_3 random error maps induced by OMI HCHO and NO_2 retrieval random errors averaged in June 2006. We use identical inputs and errors for both algorithms. Figure 5 is evidence of the diminished contamination of satellite random errors in PO_3 DNN as compared to PO_3 LASSO. The error differences tend to be larger over clean areas, because FNR random errors are higher when both HCHO and NO_2 levels are small.

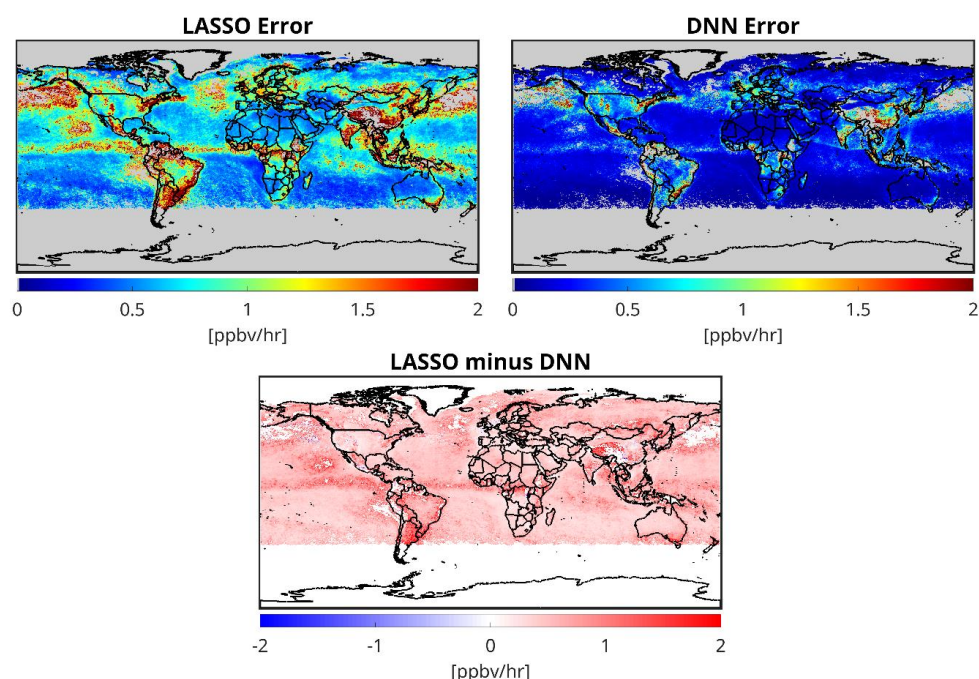


Figure 5. The comparison of the effect of satellite random errors in HCHO and NO_2 on PO_3 predictions based on PO_3 LASSO and PO_3 DNN algorithms in June 2006. The data used for generating these maps are based on OMI retrievals.

— *Continuity:* It is known that neural networks equipped with three hidden layers can well approximate almost any high-dimensional non-linear function (Shen et al., 2021). An important superiority of PO_3 DNN over PO_3 LASSO lies in the strength of the DNN algorithm at approximating high-dimensional non-linear relationships between PO_3 and HCHO (a proxy for VOCR), NO_2 (a proxy for reactive nitrogen), jNO_2 and jO^1D (a proxy for photochemistry), and H_2O . While some of these non-linearities were reasonably approximated in PO_3 LASSO by empirically segregating the chemical



conditions using FNR, the non-linear ozone photochemistry can go beyond the dependency on VOCs and NO_x levels. In fact, the relationship between PO_3 and VOCs and NO_x can behave non-linearly depending on the available light and water vapor as discussed in Section 4.3. This indicates that traditional linear models, such as those using VOCR/NO_x (or HCHO/NO_2) ratios, often fall short in capturing this complexity because of the continuous and non-linear nature of these relationships.

4.3. ***PO_3 DNN can capture non-linear PO_3 chemistry as a function of pollution, light, and humidity***

To further elaborate on the capability of PO_3 DNN to reasonably respond to variations in its five major parameters in a mathematically continuous fashion, we create six isopleths, each specifically designed to represent a particular atmospheric condition listed in Table 2. These isopleths are based on perturbing HCHO and NO_2 in PO_3 DNN and are shown in Figure 6.

It is immediately apparent that the hyperbolic shape of the PO_3 curve relative to NO_2 and HCHO can be recreated by our algorithm, displaying a positive response to both HCHO and NO_2 on the right and left sides of the ridgelines. This observation underscores the effective parametrization of the non-linearities in ozone photochemistry achieved through the DNN algorithm. In the subplot representing normal conditions, we overlaid three lines indicating FNR values of 1.5 (blue), 2.5 (green), and 3.5 (cyan). Souri et al. (2025) used these lines to determine various coefficients in the PO_3 LASSO parameterization. For instance, the derivative of PO_3 with respect to NO_2 was determined to be -0.14 ppbv/hr for $\text{FNR} < 1.5$ but increased to 6.54 ppbv/hr for $\text{FNR} > 3.5$. However, in practice, the thickness and curvature of the PO_3 isobars vary based on the prevailing atmospheric conditions, implying that the derivatives cannot consistently retain the same values across the broad range of conditions.

In bright conditions, not only do we observe a significantly accelerated response of PO_3 compared to the norm at identical NO_2 and HCHO concentrations, but the responses of PO_3 to these two compounds also become more pronounced. Conversely, in dim conditions, both the magnitudes and responses are weaker.

The contrast between dry and humid isopleths suggests that the presence of $\text{H}_2\text{O}(\text{v})$ enhances PO_3 when abundant NO_2 and HCHO are present. This trend is similarly observed in the F0AM model, as depicted in Figures S2, indicating that an increase in $\text{H}_2\text{O}(\text{v})$ over polluted regions (arbitrarily defined as $\text{HCHO} \times \text{NO}_2 > 10$) increases PO_3 . Nonetheless, more humidity suppresses PO_3 especially where VOC is limited and NO_2 is elevated possibly because the generated OH molecules from $\text{O}^1\text{D} + \text{H}_2\text{O}(\text{v})$ predominantly react with elevated NO_2 .

Lastly, we see the highest PO_3 rates recorded among all scenarios under a hypothetical condition characterized by high humidity and photolysis rates. This condition is rare in nature because large amounts of $\text{H}_2\text{O}(\text{v})$ (0.8×10^{18}) are confined to marine regions where surface reflectivity is low; nonetheless, an intuitive tendency from PO_3 DNN suggests that the algorithm does not create non-physical extrapolation values.



Table 2. Six different atmospheric conditions defined to understand the response of PO₃ to HCHO and NO₂ changes.

Labels	H ₂ O [molec/m ³]	jO ¹ D [1/s]	jNO ₂ [1/s]	Notes
<i>Norm</i>	0.4×10 ¹⁸	4×10 ⁻⁵	1.2×10 ⁻²	A typical condition in summer in the eastern US at noon
<i>Bright</i>	0.4×10 ¹⁸	7×10 ⁻⁵	1.4×10 ⁻²	Central America with abundant sunshine in the afternoon
<i>Dim</i>	0.4×10 ¹⁸	3×10 ⁻⁵	0.7×10 ⁻²	Scandinavia in the afternoon summer
<i>Dry</i>	0.1×10 ¹⁸	4×10 ⁻⁵	1.2×10 ⁻²	An arid region such as Spain Meseta Central in the afternoon summer
<i>Humid</i>	0.8×10 ¹⁸	4×10 ⁻⁵	1.2×10 ⁻²	A place the like Persian Gulf with high humidity and abundant sunshine
<i>Humid and Bright</i>	0.8×10 ¹⁸	7×10 ⁻⁵	1.4×10 ⁻²	Since accelerated photolysis rates close-to-surface usually occur over bright regions (arid) with low humidity, this condition is rare in nature.

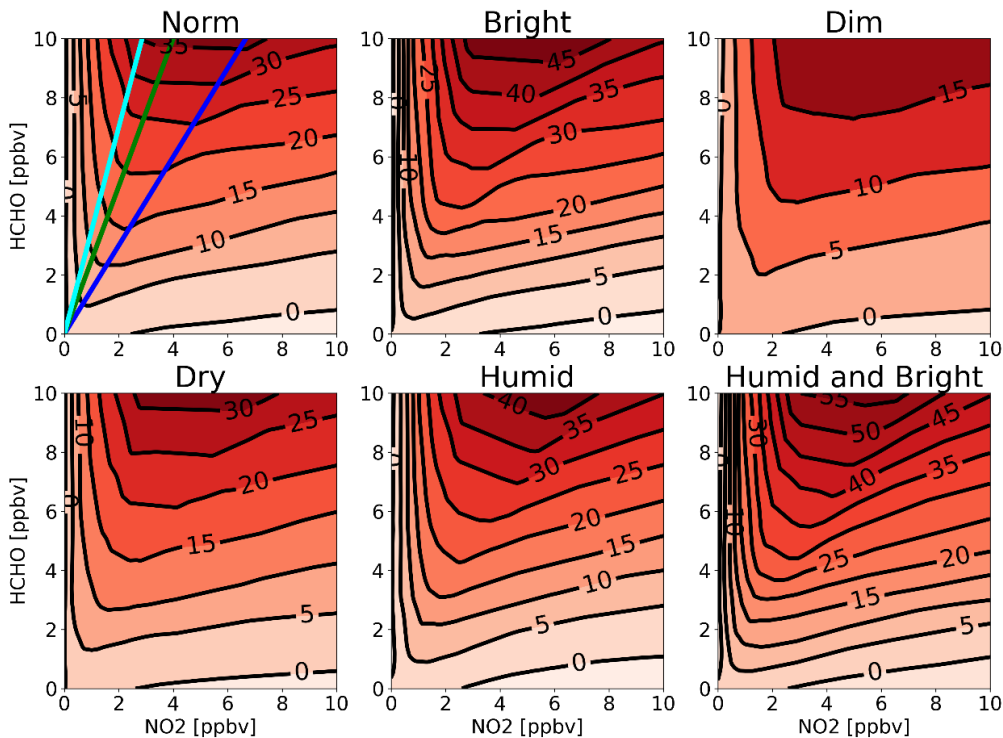




Figure 6. The contour maps of PO_3 isopleth generated by PO_3DNN algorithm for six different atmospheric conditions defined in Table 1. In the first subplot, blue, green, and cyan lines indicate $\text{FNR}=1.5, 2.5,$ and $3.5,$ respectively. Numbers on isobars are in ppbv/hr .

4.4. PO_3 Maps using OMI and TROPOMI: A General View and Anomalous Changes

4.4.1. Global PO_3 and Seasonality using OMI in 2005-2007

Figure 7 shows the global distribution of PO_3 rates averaged over a quarter-degree in 2005-2007, using OMI HCHO and NO_2 retrievals. It also includes whisker-box plots highlighting seasonal variations in PO_3 for selected regions and cities. We selected the 2005-2007 timeframe for this analysis because the OMI data were free from degradation issues, including the row anomaly. The map indicates accelerated PO_3 rates across heavily polluted regions, such as cities in the Middle East, Asia, the U.S., Central Europe, and Africa, aligning with what we observed in Sourì et al. (2025). While some areas exhibit significant seasonal fluctuations, others show little variability throughout the seasons. Notably, the east coast of the U.S., Central Europe, China, Tehran, and Johannesburg experience peak PO_3 rates in summer. This pattern is primarily attributed to enhanced photochemistry and the elevated sensitivity of PO_3 to NO_x , driven by increases in VOCR/NO_x (Sourì et al., 2025).

The seasonal variability of PO_3 in two African regions, characterized by biomass burning, exhibits an anti-correlation. This occurs because biomass burning in the northern hemisphere of Africa occurs from November to March, while the southern hemisphere in Africa experiences it from June to September (Roberts et al., 2009). Southeast Asia also shows a peak in PO_3 during the biomass burning season (August-September).

Places like Mexico City, several major Brazilian cities (including Sao Paulo and Rio de Janeiro), northern India, and the southwest coast of the U.S. show minimal seasonal variability in PO_3 . The lack of pronounced seasonal changes may be attributed to less pronounced fluctuations in photolysis rates or substantial spatial heterogeneity in the seasonal variabilities of HCHO and NO_2 , resulting in reduced seasonal variations but with greater variance. Nonetheless, certain weather conditions can influence these results; for instance, monsoon flows can disperse and scavenge pollution from the northern India around July-September (David and Nair, 2013), dampening PO_3 . Mexico City also experiences a monsoon season in summer causing pollution to subside temporarily. The attribution of the seasonality will be discussed in the next section.

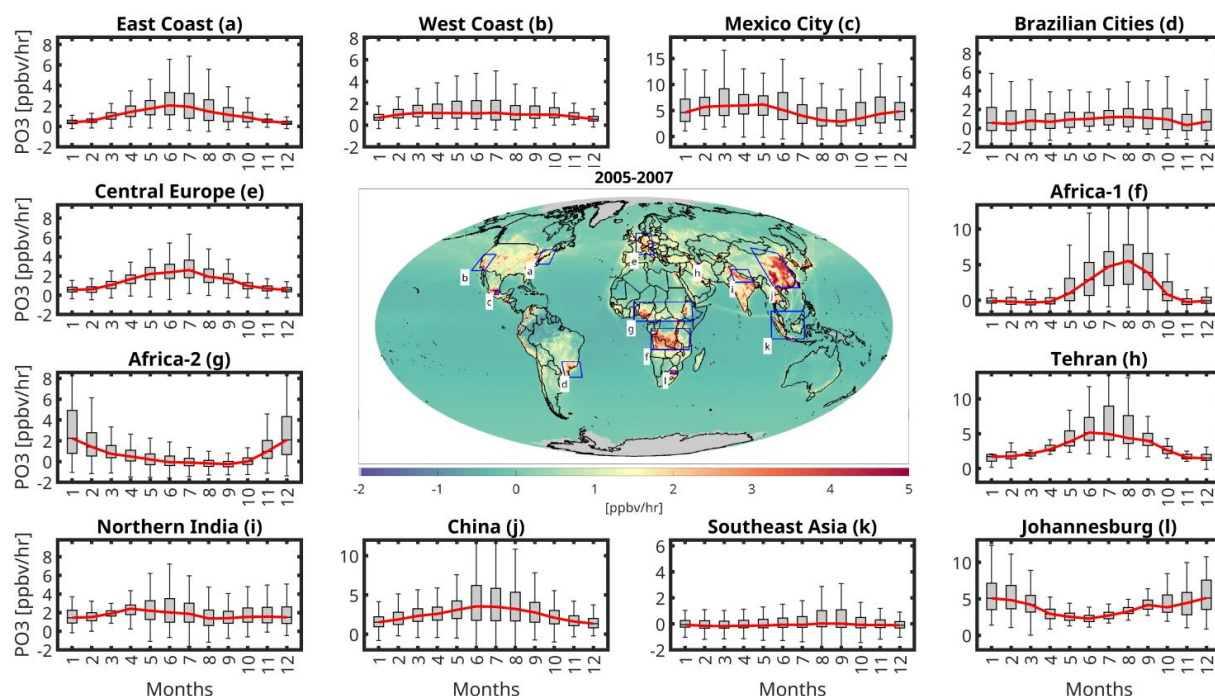


Figure 7. (center) The averaged global PO_3 map at $0.25^\circ \times 0.25^\circ$ in 2005-2007 based on the new algorithm. OMI data are used to populate HCHO and NO_2 abundance. (margins) the whisker-box plots of PO_3 seasonality over various selected regions. In the box plot, the central red line shows the median, and the top and bottom edges of the box show the 25th (q_1) and 75th (q_3) percentiles. The dark solid lines at the very beginning and the end of each plot show the minimum and maximum values excluding the outliers. The outliers are removed based on by any value above $q_3 + 1.5 \times (q_3 - q_1)$ or below $q_1 - 1.5 \times (q_3 - q_1)$.

4.4.2. The attribution of PO_3 seasonality

Photolysis rates, which serve as crucial indicators of photochemical activity, are the primary determinants of PO_3 seasonality. Figure 8 illustrates the sensitivity of PO_3 to NO_2 , HCHO , and combined J-values ($j\text{NO}_2$ and $j\text{O}^1\text{D}$) based on Eq.3 across the same regions and months presented in Figure 7. The absolute values of PBL HCHO , NO_2 , and $j\text{NO}_2$ are shown in Figure S3. As shown in Appendix A, these sensitivity values are influenced by both the magnitude of the precursor and the first derivative of PO_3 with respect to that precursor. Thus, the sensitivity values should be interpreted as the result of these combined effects.

The amplitude of photolysis rates dictates the amplitude of the sensitivity of PO_3 to NO_2 and HCHO . For instance, over East Coast, Central Europe, and Tehran, the first derivative of PO_3 to NO_2 tends to be small during colder months, primarily because of reduced photochemistry and non-linear chemistry. As a result, despite significantly higher NO_2 concentrations in these months, the sensitivity of PO_3 to NO_2 is muted; this tendency indicates that the derivative effect can overshadow the increase in NO_2 concentrations. Conversely, in warmer months, the larger positive derivative of PO_3 relative to NO_2 , driven by increased HCHO levels (shifting away from VOC-sensitive regimes) and enhanced photolysis rates, markedly increases the contributions of low summer NO_2 levels to PO_3 . Likewise, we observe substantially higher sensitivity of PO_3 to HCHO concentrations during warmer seasons. This increase is attributed to



both the elevated levels of HCHO and the growing derivative of PO_3 with respect to HCHO, both of which are directly influenced by enhanced photochemistry. One might argue that summer conditions should lead to a shift towards extremely NO_x -sensitive regimes, resulting in a reduced first-order derivative of PO_3 to HCHO. However, most polluted regions chosen for this figure are in transitional regimes during the summer, which renders PO_3 fairly responsive to HCHO concentrations. These results underscore the importance of including photolysis rates in ozone sensitivity analysis, rather than relying solely on FNR in former studies. For example, a lower FNR in the morning (~0930 LST) compared to the afternoon may wrongly suggest that PO_3 would become more sensitive to VOCs earlier in the day. However, decreased light in the morning reduces the sensitivity of PO_3 to VOCs, despite a lower FNR.

The sensitivity of PO_3 to photolysis rates is dependent on pollution levels, just as its sensitivity to HCHO and NO_2 concentrations is influenced by photolysis rates. This is primary reason for seeing minimal seasonality of PO_3 over Mexico City, various Brazilian cities, and northern India. These minimal changes in photolysis rate sensitivities are caused by the less pronounced seasonality in both photolysis rates and pollution levels compared to other areas (Figure S3). Souri et al. (2025) found that photolysis rates significantly contribute to the production of PO_3 when there is an adequate amount of ozone precursors. This was reflected in larger coefficients associated with photolysis rates in PO_3 LASSO algorithm for $\text{FNR} < 1.5$, where pollution levels were high. For example, high photolysis rates over the Sahara do not significantly contribute to PO_3 because of the limited availability of ozone precursors needed to initiate the RO_x - HO_x cycle. A notable example can be observed in Africa, where photolysis rates tend to remain consistent throughout the year under near cloud-free conditions (Figure S3). However, there is a marked seasonality in the sensitivity of PO_3 with respect to photolysis rates during polluted months suggesting that the ample precursors can leverage available lights to form more ozone molecules. This pattern underscores the algorithm's capability to understand the intertwined relationships between the photolysis rate sensitivities and pollution levels, as well as the pollution sensitivities and photolysis rates.

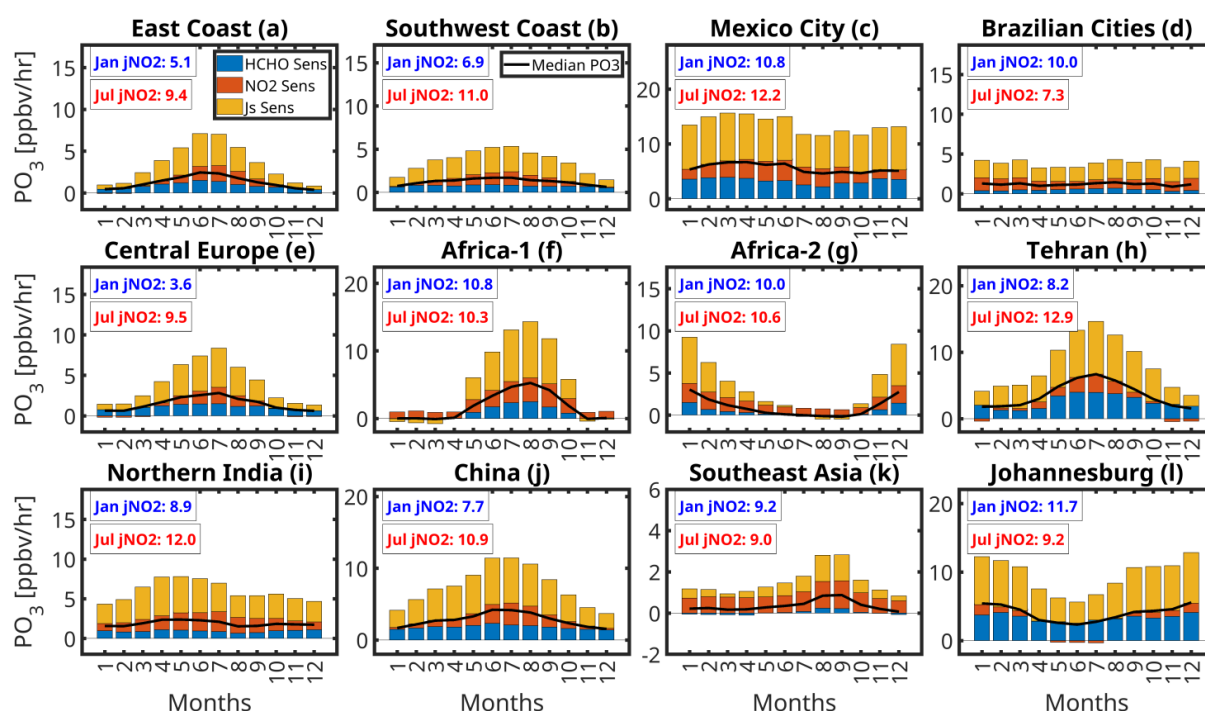




Figure 8. The bar plots of the sensitivity of PO_3 to photolysis rates, NO_2 , and HCHO concentrations within the PBL over the selected regions shown in Figure 7. These sensitivities are influenced by both the magnitude of the precursors and the first-order derivative of PO_3 to the precursor, detailed in Appendix A. jNO_2 values are in $1 \times 10^3/\text{s}$ units.

4.4.3. Can rapid heatwaves accelerate PO_3 in the northeast U.S.?

Heatwaves are known to worsen ozone pollution in many regions because of several factors. Increased temperatures can elevate both anthropogenic and biogenic VOCs (Guenther et al., 2012; Wu et al., 2024). Additionally, higher temperatures can accelerate some key reaction rates, particularly $\text{NO} + \text{RO}_2$ (Pusede et al., 2015). Longer periods of active photochemistry can occur because of fewer clouds, and the dispersion of ozone and its precursors may be hindered by a dominant high-pressure system (Pyrgou et al., 2018). However, some of these effects may be offset if heatwaves last for an extended period, as drought conditions can suppress biogenic VOCs (Duncan et al., 2009; Demetillo et al., 2019). In this study, we focus on a severe heatwave that affected the eastern U.S. in August 2007. To contrast the atmospheric conditions during this month with those of a typical condition, we use August 2008 as a baseline.

Our PO_3 DNN product shown in Figure 9 exhibits a 21% increase in PO_3 rates with respect to the baseline throughout the northeast U.S., suggesting that rapid heatwaves can accelerate the production of chemically-generated ozone molecules. It is important to acknowledge that both maps represent conditions with minimal cloud cover imposed by the cloud-screening flags from the satellite retrievals. However, the frequency of clear-sky conditions is usually higher during heatwaves compared to normal conditions. This distinction is critical because clouds play a significant role in reducing photochemical activity close to the surface by limiting incoming solar radiation. Consequently, even if PO_3 values appeared similar between these two episodes, the more frequent occurrence of clear-sky conditions in August 2007 would result in a greater cumulative contribution of PO_3 to the region. This highlights the impact of persistent sunshine in enhancing ozone, reinforcing the need to account for meteorological variability when analyzing photochemical processes.

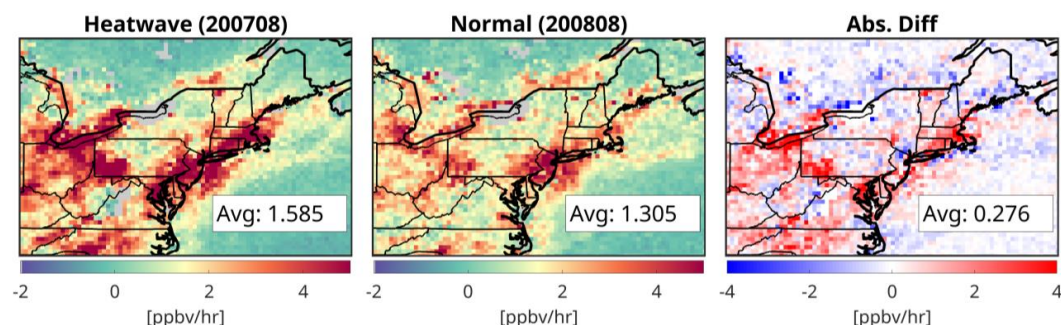


Figure 9. The maps of PO_3 within PBL in August 2007 (left), August 2008 (middle), and their absolute difference (right).

To study the reasons behind the accelerated PO_3 during this episode, we explore the respective changes in ozone precursors and the sensitivities by the heatwave. Figure 10 contrasts the differences in NO_2 and HCHO levels within the PBL region for two episodes. These maps are derived from the bias-corrected OMI VCDs scaled to the PBL region using MINDS simulations. Different wind patterns are most likely the cause of the differences in NO_2 patterns over cities; we see different shapes of NO_2 plumes over NYC, Toronto, and Boston. Additionally, we see some uniform enhancements of NO_2 in several inland regions, such as Washington DC, Philadelphia, North Carolina, Tennessee, and Ohio. While we cannot definitively locate the cause of these enhancements without additional measurements and models, we can speculate that rising temperature can increase both nitrification and denitrification microbial activities under



optimal soil moisture causing soil NO_x emissions to rise. Another possible explanation could be that NO_x reservoirs (such as PAN and alkyl nitrate) can rapidly be converted back to NO_2 because of higher temperature and more sunshine. HCHO levels are markedly high during the heatwave event in comparison to the baseline (>2 ppbv). The enhanced biogenic emissions and photochemistry are the causes.

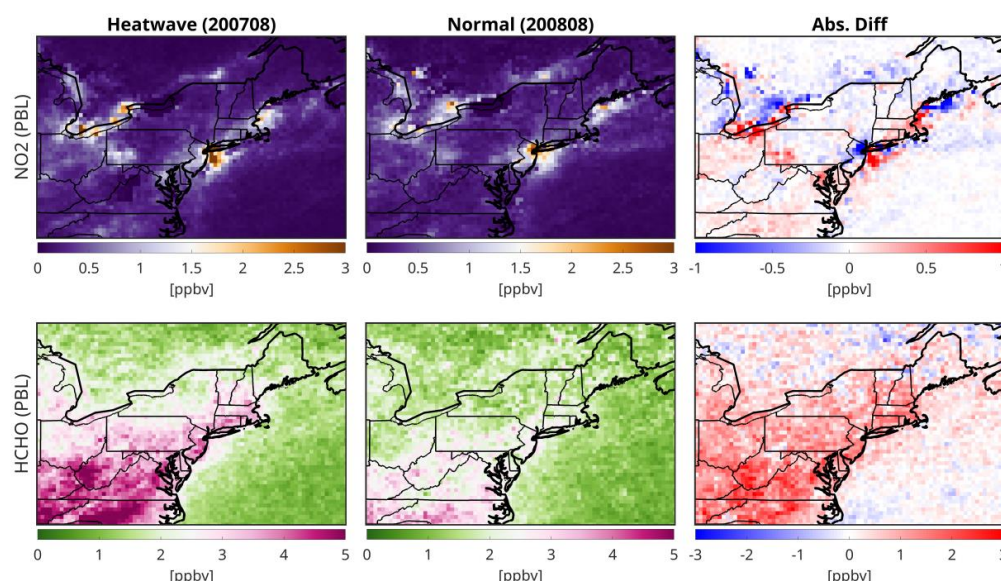


Figure 10. The maps of NO_2 (top) and HCHO (bottom) concentrations within PBL averaged in month of August in 2007 (heatwave) and 2008 (a normal condition), and their absolute differences. The abundance of HCHO and NO_2 are informed by bias-corrected OMI retrievals.

Using the spatially-varying sensitivity of PO_3 to NO_2 and HCHO provided by our product, we find that in rural and suburban areas, the derivative of PO_3 to NO_x tends to be high (NO_x -sensitive regimes) (Figure 11), indicating that even a small increase in NO_2 in several inland regions can boost the sensitivity of PO_3 to NO_2 greatly. This observation is consistent with findings from Geddes et al. (2022), who reported a similar trend of increasing ozone sensitivity to soil NO_x emissions across various remote regions in the U.S.

We observe that higher levels of HCHO significantly increase the sensitivity of PO_3 to HCHO in several high- NO_x areas, including Toronto, Boston, Washington DC, Philadelphia, and Buffalo, as illustrated in Figure 11. As noted before, the sensitivity maps are influenced by both the magnitude of a precursor and the derivative of PO_3 with respect to a precursor. In high- NO_x regions, the derivative of PO_3 to HCHO is typically large (i.e., VOC-sensitive). Consequently, elevated HCHO concentrations lead to a greater sensitivity of PO_3 to HCHO levels. Conversely, in remote regions where the derivative of PO_3 to HCHO is small, increases in HCHO cannot induce noticeable effect on PO_3 . An exception to the general increase in PO_3 sensitivity to HCHO occurs over NYC. This anomaly can be attributed to the different shape of the NO_2 plume in August 2008 as compared to 2007. In August 2007, as shown in Figure 10, NO_2 concentrations in NYC were dispersed over the ocean, resulting in less VOC-sensitive conditions (lower derivative of PO_3 to HCHO) within the city. As a result, PO_3 sensitivity values to HCHO decrease because the first-order derivative decreases.

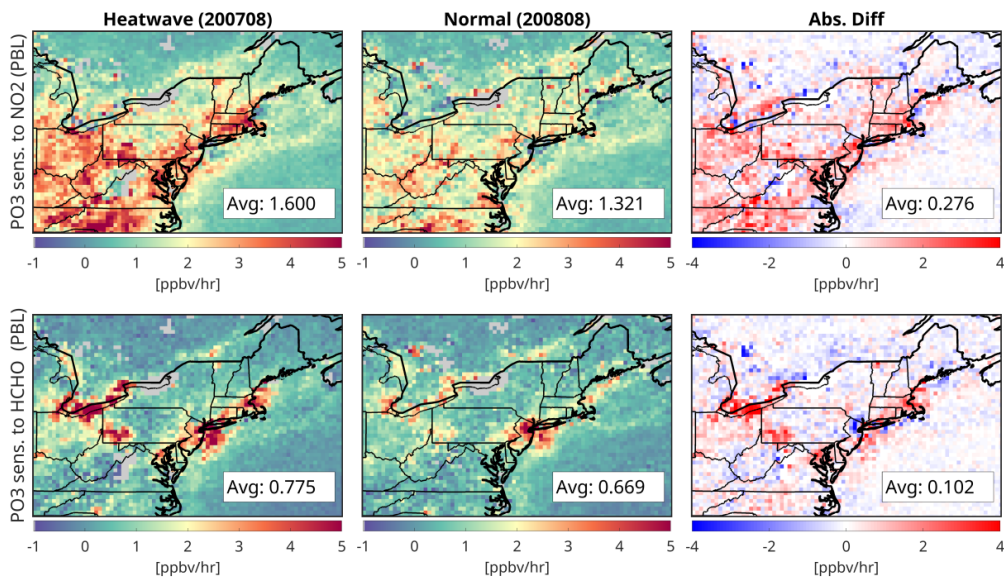


Figure 11. A similar layout as shown in Figure 10, but with the sensitivity outputs derived from the PO₃DNN algorithm.

4.4.4. High resolution TROPOMI-based PO₃ maps and sensitivities contrasted with OMI

Accelerated rates of PO₃ at approximately 1330 LST are observed consistently across polluted midlatitude regions characterized by high photolysis rates. This pattern is substantiated by the global PO₃ maps derived from TROPOMI and OMI data for the year 2019 illustrated in Figure 12. While the maps presented are averages for 2019, significant PO₃ hotspots (exceeding 8 ppbv/hr) are identified over metropolitan/industrial areas including Mexico City (Mexico), Tehran (Iran), the Persian Gulf, and Hunan Province (China). There are less documented regions undergoing elevated locally-produced ozone such as Johannesburg (South Africa), Rio de Janeiro (Brazil), Sao Paulo (Brazil), and Santiago (Chile). In contrast, Europe emerges as a region with comparatively low PO₃ levels despite its dense population. This tendency may be attributed to lower photolysis rates (characterized by high solar zenith angles and low surface reflectivity) as well as effective emissions mitigation strategies. A notable similarity exists between these identified hotspots and those reported by Souri et al. (2025), although the contrast between clean and polluted areas is more pronounced in the PO₃DNN product because of an improved representation of PO₃DNN in clean regions.

PO₃ exhibits a slight negative value over oceanic and densely forested areas (such as the Amazon and Congo), primarily because of ozone sinks associated with water vapor (H₂O(v)) and alkenes, which are implicitly included in our parametrization. However, a marked contrast is observed between the slightly negative and positive PO₃ levels along marine vessel pathways. These ship paths are informed not only by remote sensing data (Georgoulas et al., 2020) but also by the conversion of column measurements to PBL mixing ratios thorough the MINDS simulation, which accounts for ship emissions. Given that the PBL is typically shallow over marine regions, the conversion factor is expected to be substantial for these pathways, resulting in a pronounced contrast in pollution levels within the PBL.

The finer spatial resolution of the TROPOMI dataset enhances the detail of the PO₃ maps compared to those derived from OMI, yielding less noise and fuller data. This reduction in gaps in TROPOMI-based PO₃ is attributed to a lower likelihood of cloud contamination and the full coverage of all detectors, in



717 contrast to OMI, which suffers from the row anomaly. Visual analysis of the two datasets indicates that
718 TROPOMI consistently shows higher PO_3 than OMI over polluted regions. Except for NO_2 and HCHO
719 VCDs, the inputs to the parametrization are identical across both products.

720 To further investigate these differences, we synchronized the TROPOMI datasets at the OMI-based
721 spatial resolution and produced scatterplots, as displayed in Figure 13. The correspondence between the
722 two products is high ($R^2 = 0.86$). Nonetheless, TROPOMI-based PO_3 levels are approximately 10% greater
723 than those derived from OMI. The fact that we observe this overestimation given that TROPOMI has been
724 coarsened to match OMI's footprint suggests that the differing spatial resolutions (0.25 degrees versus 0.1
725 degrees) are unlikely to account for the discrepancy. Moreover, we undertake a comparative analysis of
726 NO_2 and HCHO mixing ratios within the PBL region as obtained from MINDS alongside these two satellite
727 datasets. Given that the conversion factor remains consistent between the two products, any observed
728 differences can be attributed to variations in their respective VCDs. Our analysis reveals that both NO_2 and
729 HCHO mixing ratios are higher in TROPOMI relative to OMI (by 5-6%), thereby providing a solid
730 explanation for the elevated TROPOMI-based PO_3 in comparison to OMI.

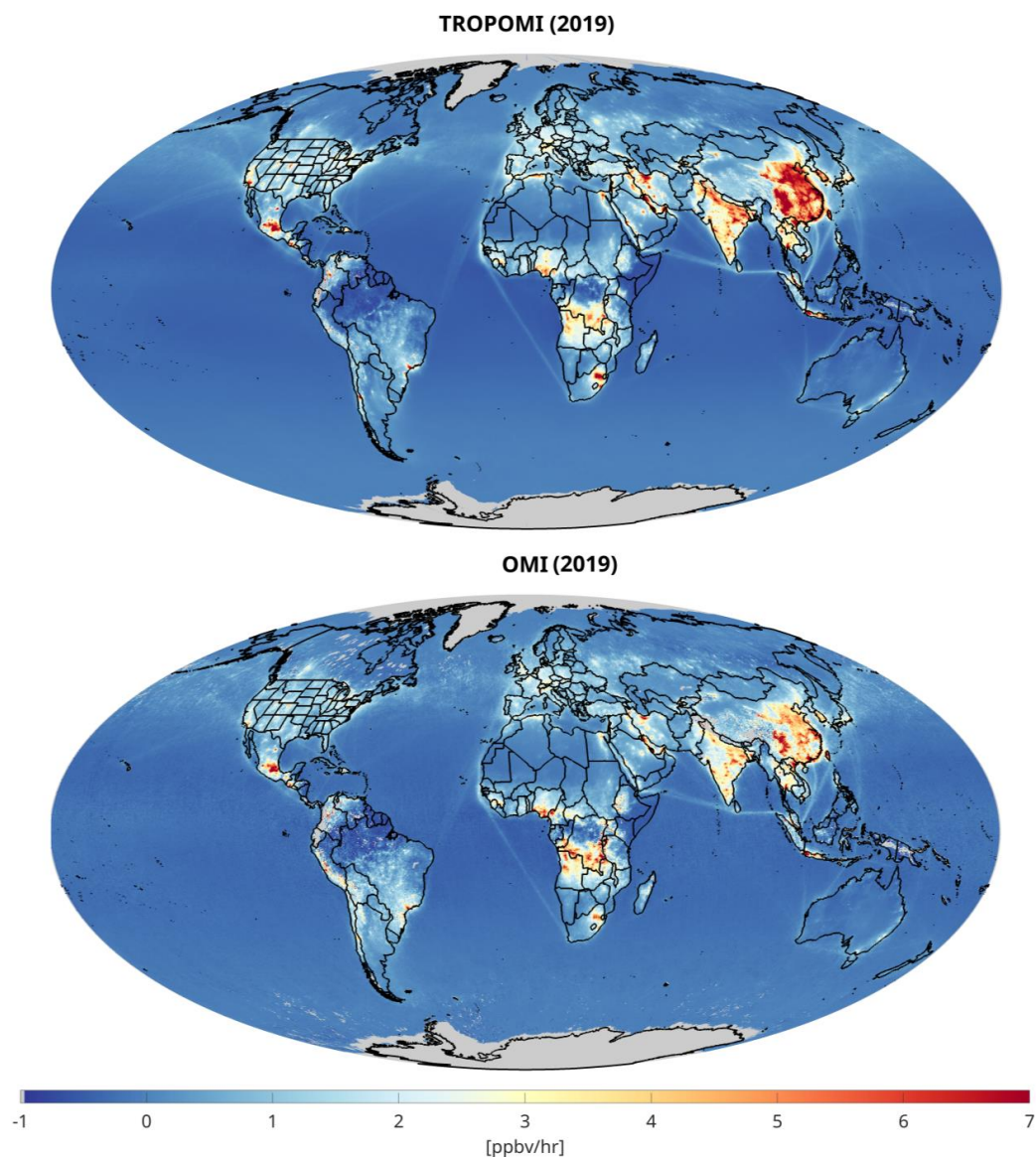
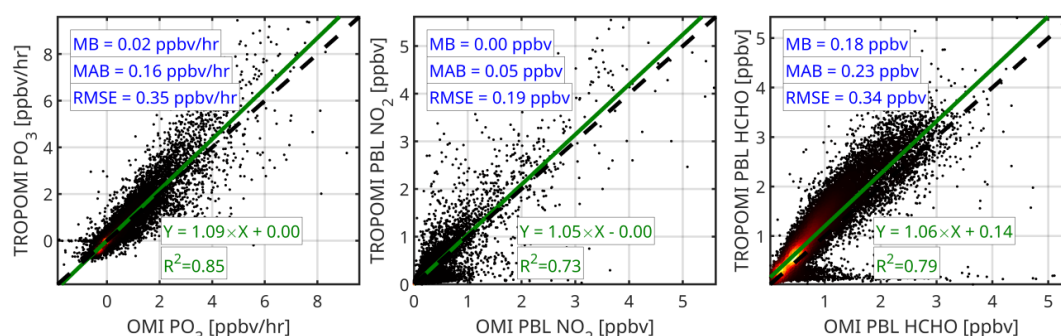


Figure 12. Global maps of PO_3 derived from TROPOMI (top) and OMI (bottom) datasets based on the PO_3 DNN algorithm in 2019. These values are estimated within the PBL region at ~1330 LST. The data exclude cloudy pixels, strong smoke, sensor anomalies, and snow based on the recommended quality flags coming with TROPOMI and OMI products.

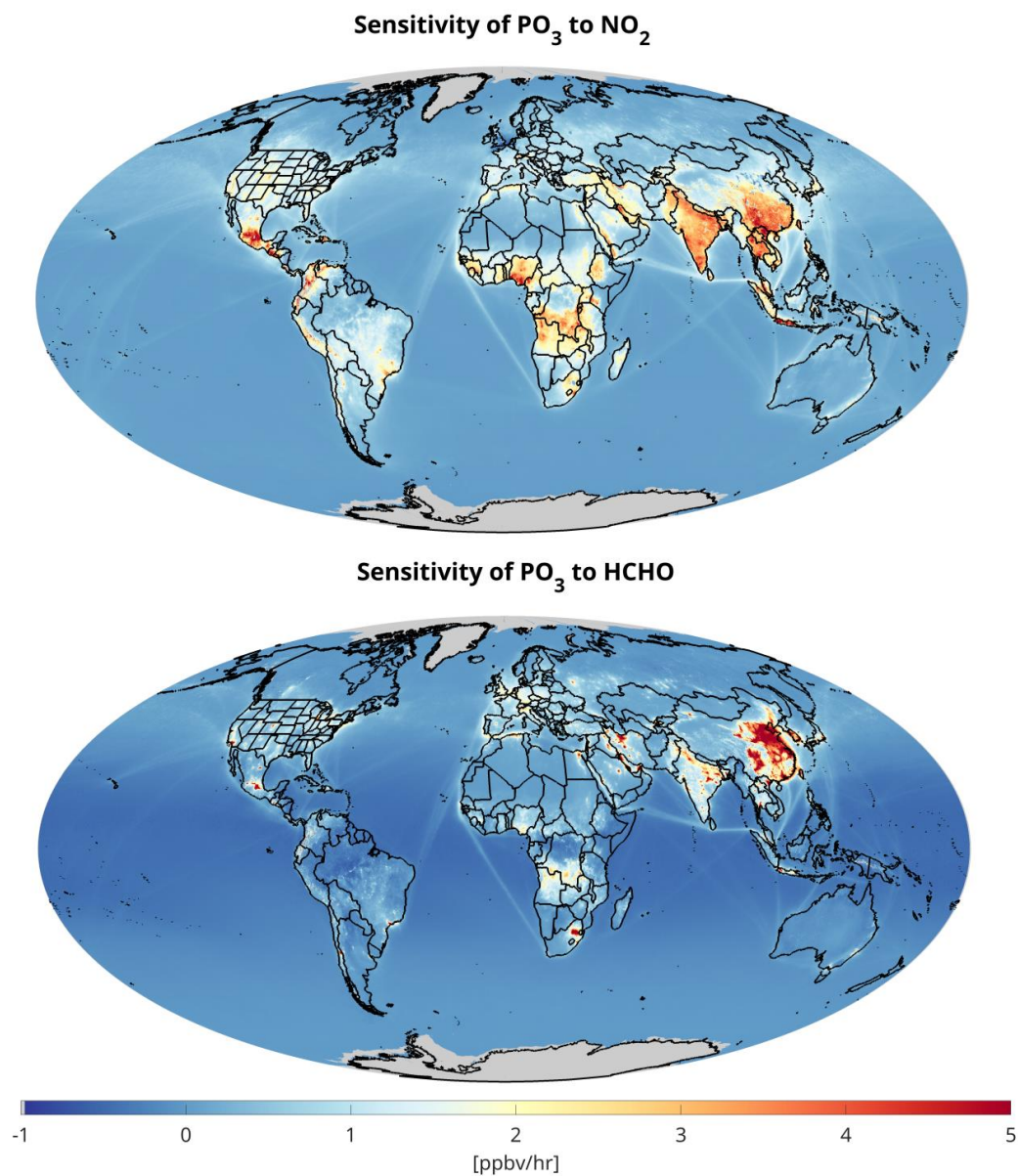


738

739 **Figure 13.** Scatterplots of (left) OMI PO₃ vs. TROPOMI PO₃, (middle) OMI PBL NO₂ vs. TROPOMI PBL
 740 NO₂, and (right) OMI PBL HCHO vs. TROPOMI PBL HCHO based on 2019. We coarsen TROPOMI
 741 dataset to match OMI's spatial resolution to remove the effect of spatial footprint on these results.

742 We explore the spatially varying sensitivity of PO₃ to HCHO and NO₂ worldwide. These maps
 743 provide finer information compared to binary maps obtained from FNRs. Figure 14 illustrates global maps
 744 of these sensitivities averaged for the year 2019. We observe negative sensitivity values of PO₃ to NO₂ in
 745 urban areas, which aligns with our understanding of non-linear ozone chemistry. These negative values are
 746 particularly pronounced in northern China, where VOC/NO_x ratios remain low throughout the year. Similar
 747 non-linear feedback patterns can be seen in the Benelux region and the United Kingdom, primarily driven
 748 by elevated NO₂ levels. In contrast, NO₂ significantly contributes to higher PO₃ levels in southern China,
 749 India, Mexico, and several regions across Africa.

750 As indicated in Sourì et al. (2025), the influence of HCHO on PO₃ is largely governed by NO_x
 751 emissions. This relationship explains why the sensitivity of PO₃ to HCHO closely mirrors global NO₂ levels,
 752 which dictates the locations of VOC-sensitive regimes. We observe slightly negative sensitivity of PO₃ to
 753 HCHO in remote and densely vegetated regions, likely a result of the effects of alkenes on ozone. However,
 754 the implicit nature of DNN makes it challenging to identify the exact chemical reasons behind these
 755 patterns. Noteworthy examples of areas where PO₃ is significantly influenced by HCHO include eastern
 756 China, Los Angeles (USA), Tehran (Iran), Mexico City (Mexico), and Johannesburg (South Africa).



757

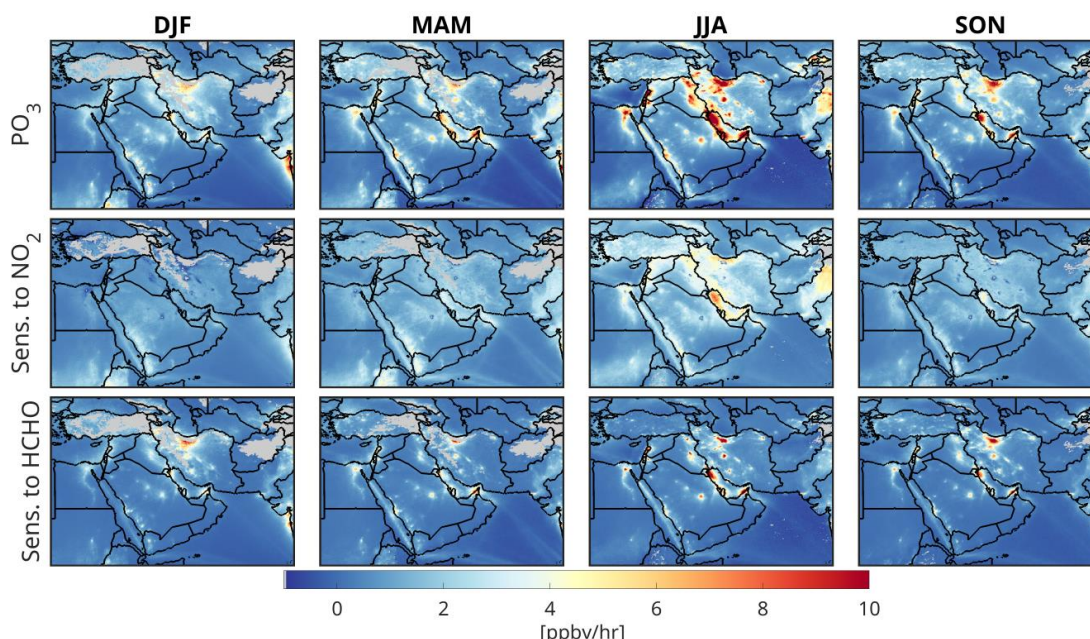
758 **Figure 14.** The sensitivity of PO_3 to NO_2 (top) and HCHO (bottom) based on our algorithm using
759 TROPOMI data in 2019.

760

761



Figure 15 presents the maps of PO_3 along with sensitivities across four seasons in 2019 over Middle East, derived from TROPOMI data. Notably, PO_3 values surge during the summer months in several densely populated and industrial regions of the Middle East. Furthermore, we observe considerable PO_3 values in the fall, primarily caused by the influence of HCHO. This fall peak is consistent with the observations made by Souri et al. (2025), who reported a sharp rise in PO_3 in late fall 2019 over Tehran (Iran). The overall seasonality of PO_3 is well aligned with the discussions presented in Section 4.4.1. The sensitivity of PO_3 to NO_2 exhibits notable variation, shifting from low and negative values during the colder months to positive and high values in the warmer months. We identify HCHO as the predominant contributor to PO_3 in these regions, as the majority of these cities fall in VOC-sensitive environments and emit significant amounts of anthropogenic HCHO, whether from primary or secondary sources. These maps eliminate the need for binarization of chemical conditions, as they effectively illustrate the spatial variability in ozone response to HCHO and NO_2 .



77.

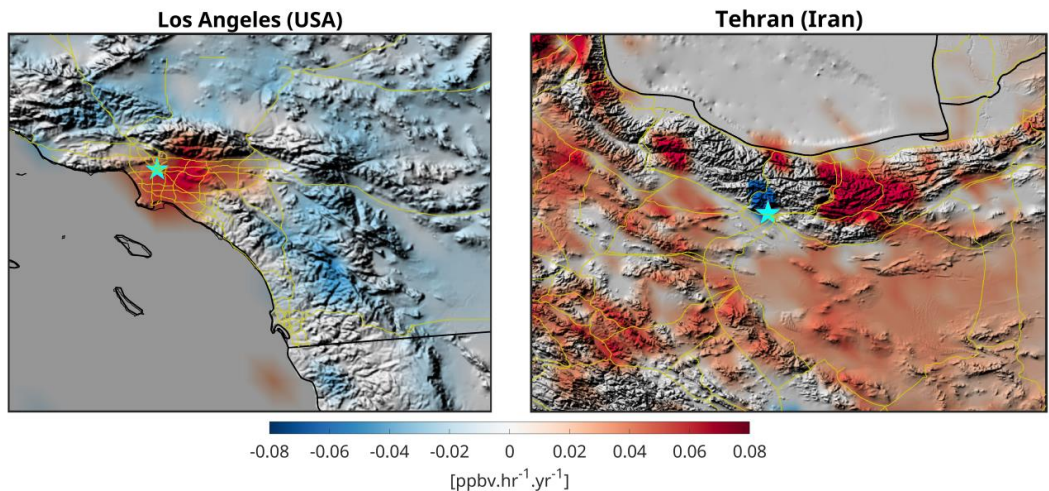
Figure 15. The magnitude of PO_3 and the corresponding sensitivity to NO_2 and HCHO over Middle East grouped into four different seasons. DJF: December-January-February, MAM: March-April-May, JJA: June-July-August, and SON: September-October-November. *Sens.* means sensitivity.

4.4.5. A Tale of Two Cities: Long-term trends of PO_3 in Los Angeles vs. Tehran in 2005-2019

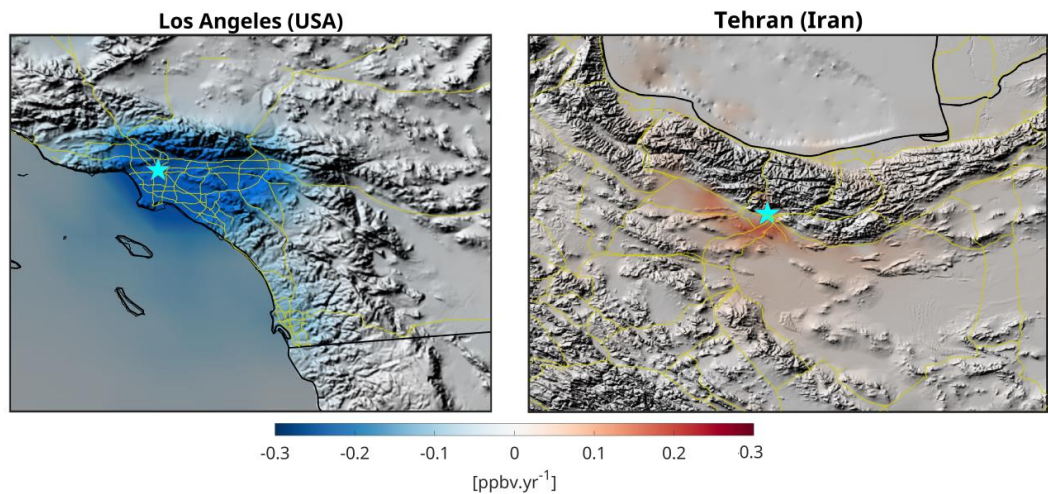
Using a linear trend calculation method outlined by Souri et al. (2024), we evaluate the long-term linear trends of PO_3 maps in two cities: Los Angeles (USA) and Tehran (Iran). Figure 16 clearly demonstrates a complete reversal in the linear trends of PO_3 , revealing an increase in Los Angeles and a decrease in Tehran. Moreover, we observe similar contrasting trends in the surrounding areas, with PO_3 levels rising near Tehran while declining near LA (Los Angeles). This tendency is a textbook example of non-linear ozone chemistry. While we do not identify any statistically significant trends in HCHO mixing ratios within the PBL for these two major cities, we do observe a significant downward trend in NO_2 mixing ratios in Los Angeles and a substantial upward trend in Tehran, as illustrated in Figure 17. Since both cities are primarily in VOC-sensitive conditions at their cores (Souri et al., 2025), it is intuitively clear a reduction (enhancement) in NO_2 should lead to positive (negative) trends in PO_3 because of the impact of the loss of



789 NO_x on PO₃. Conversely, in their suburbs where the negative effect of the loss of NO_x on PO₃ diminishes,
790 we see a close association of the sign of PO₃ trends and those of NO₂.
791



792
793 **Figure 16.** The statistically significant linear trends of PO₃ over LA (left) and Tehran (right) based on the
794 PO₃DNN product in 2005-2019.
795



796
797 **Figure 17.** The statistically significant linear trends of PBL NO₂ mixing ratios over LA (left) and Tehran
798 (right) based on the bias-corrected OMI and MINDS product in 2005-2019.

799 **4.5. Error Analysis**

800 Based on the formulation outlined in Section 3.4, we evaluate both the systematic and random error
801 components of PO₃ for July 2019, based on data from both OMI and TROPOMI retrievals. Figure 18
802 presents the average error values for the month. Total PO₃ errors range from 25% to 80% in areas
803 characterized by moderate to extreme pollution, while in more remote regions, errors can surpass 200%.



On average, random errors constitute only a small fraction of the total error budget, with OMI showing consistently larger random errors than TROPOMI across the region. This is primarily a result of OMI's limited sampling caused by row anomaly issues. As mentioned in Section 4.2, these random errors are significantly lower when compared to the PO₃LASSO random errors (Souri et al., 2025).

Systematic errors account for most of the total error, exceeding 90%. These systematic errors are comprised of three components: biases arising from the correction of VCDs using ground-based remote sensing data, errors related to DNN predictions, and conversion factors derived from the MINDS framework. The first two components contribute minimally to the overall error (less than 5%), making the MINDS conversion factors the dominant contributor to the total error budget. Therefore, any parametrization aimed at converting satellite-based VCDs to near-surface concentrations, including the one presented in this study, should always seek out a model that accurately reflects the shape of the profiles.

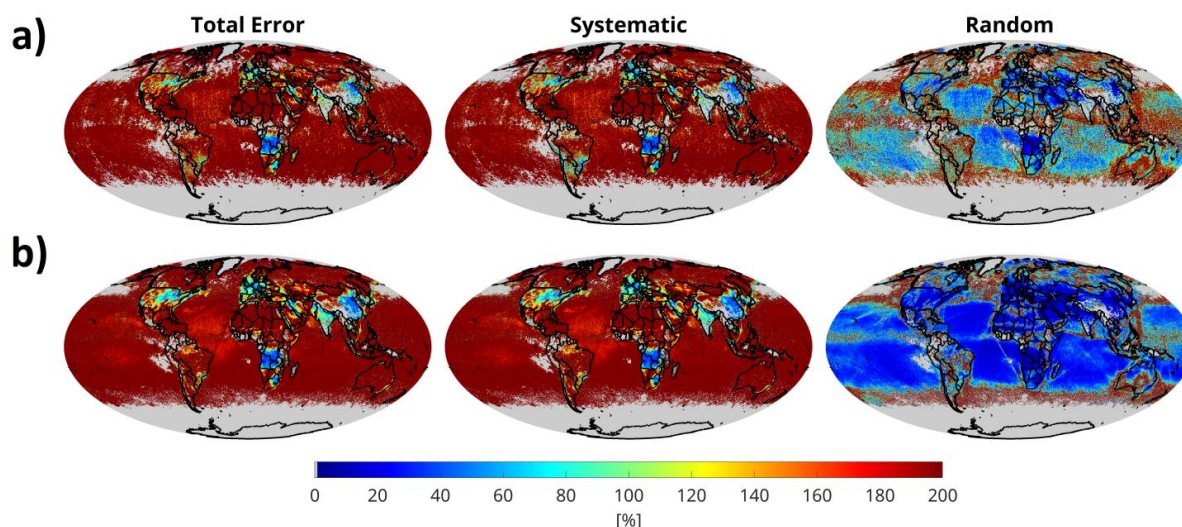


Figure 18. The maps of total error, systematic, and random errors for (a) OMI, and (b) TROPOMI computed for July 2019.

5. Summary

Early data-driven analyses of ozone chemistry sensitivity primarily relied on "ratio-based" indicators to partially linearize the non-linear aspects of urban ozone chemistry, which are influenced by pollution levels, light, and water vapor. With the development of more sophisticated algorithms, including machine learning techniques capable of fitting high-dimensional non-linear functions, we have shown that a highly effective parameterization of net ozone production rates (PO₃) can be achieved. This approach not only eliminates the need for empirical linearization of ozone chemistry through various indicators, but it also allows for the primary inputs to be accurately constrained using satellite observations. This advancement allowed us to move beyond the previously employed formaldehyde-to-nitrogen dioxide ratio (FNR) and to generate more comprehensive sensitivity maps, which account for variations not only in HCHO and NO₂ but also in light and water vapor.

We significantly enhanced the empirical parametrization of PO₃ described in Souri et al. (2025), in several key ways: (i) we improved the representation of PO₃ in both polluted and clean areas using a L2-regularized deep neural network (DNN) and eliminated the need for empirical linearization of atmospheric conditions with the FNR approach, resulting in reduced complexity and noise in the final estimates; (ii) we



833 used a finer, up-to-date global transport model called MINDS to convert satellite-retrieved vertical column
834 density (VCD) into planetary boundary layer (PBL) mixing ratios; (iii) we incorporated the error from these
835 conversion factors, derived from comprehensive validation against aircraft spirals, into the total error
836 budget; and (iv) we generated long-term records of PO_3 magnitudes and sensitivities to nitrogen dioxide
837 (NO_2) and formaldehyde (HCHO) using bias-corrected data from the Ozone Monitoring Instrument (OMI)
838 for the years 2005-2019 (at a resolution of $0.25^\circ \times 0.25^\circ$) and the TROPospheric Monitoring Instrument
839 (TROPOMI) for 2018-2023 (at a resolution of $0.1^\circ \times 0.1^\circ$). These datasets were collected under partially
840 cloud-free conditions around 13:30 equatorial local standard time. The two products show strong
841 agreement, with TROPOMI-based PO_3 being approximately 10% higher than OMI, which is attributed to
842 higher NO_2 and HCHO concentrations noted by TROPOMI.

843 The DNN algorithm (PO_3DNN) accounted for more than 96% of the variance in both the test and
844 training datasets derived from observationally-constrained box simulations across various atmospheric
845 composition campaigns, with a slope close to the unity line. The new algorithm improved the representation
846 of PO_3 in remote regions compared to the version developed in Sourì et al. (2025), due to the inclusion of
847 water vapor and the use of a more robust regression model. We found PO_3DNN to be logically responsive
848 to its inputs during various idealized experiments that involved changing light conditions, pollution levels,
849 and water vapor.

850 Expectedly, our results indicate that PO_3 magnitudes and sensitivity maps are primarily influenced
851 by the levels of ozone precursors, non-linearity of ozone chemistry, and photolysis rates. We revisited the
852 accelerated PO_3 observed in Sourì et al. (2025) across polluted areas, such as major cities and during
853 biomass burning activities in photochemically active environments. Using sensitivity calculations derived
854 from the new algorithm, we investigated the contributors to PO_3 seasonality around the globe. We found
855 that photolysis rates were the primary drivers of PO_3 seasonality. During darker months, both the magnitude
856 of PO_3 and its sensitivity to NO_2 and HCHO decrease due to limited light availability to initiate the RO_x -
857 HO_x cycle. This critical trend is not represented by the pollution levels alone, highlighting the necessity of
858 including photolysis rates in ozone sensitivity analyses. Fortunately, we can largely constrain these rates
859 using satellite observations. In regions with minimal variability in photolysis rates (such as the tropics),
860 pollution levels became the main driver of PO_3 seasonality.

861 To demonstrate the application of the algorithm for monitoring locally-produced ozone during an
862 extreme event, we compared PO_3 magnitudes and sensitivity maps during a rapid heat wave event over the
863 northeastern U.S. to a typical month. We observed a 21% increase in PO_3 across the region, primarily
864 attributed to rising background NO_2 levels, potentially resulting from enhanced soil NO_x emissions or the
865 photo- or thermal-dissociation of NO_x reservoirs, along with increases in HCHO in VOC-sensitive areas.
866 These results suggest that the rapid calculation capabilities of our product can aid in identifying the causes
867 behind unusual ozone exceedances triggered by weather events, without requiring substantial expertise or
868 computational resources for fine-tuning chemical transport models. However, it is important to note that
869 those models are essential for comprehensively understanding all physiochemical processes responsible for
870 ozone formation and loss, as they provide explicit and process-based details.

871 The long record of stable observations from OMI allowed us to generate the first-ever maps of PO_3
872 linear trends from 2005 to 2019. While a global analysis of these trend trends certainly requires a follow-
873 up study, we chose two major cities, Tehran (Iran) and Los Angeles (USA), as a showcase because they both
874 fall into the same chemical conditions but experience opposite NO_2 trends. These maps revealed a
875 contrasting trend, with Tehran exhibiting negative trends at the city center and positive trends in the
876 surrounding areas. We did not notice significant changes in HCHO, which may be due to the detection
877 limits of OMI. However, mixing ratios of NO_2 PBL markedly decreased in Los Angeles and increased in
878 Tehran, a reflection of the implementation and neglect of effective emission mitigation strategies,
879 respectively. As both cities fall into the VOC-sensitive category and are negatively correlated with NO_2
880 concentrations, the differing patterns in their PO_3 trends result from the non-linear chemistry of ozone. This



observation was reinforced by the opposite trends in the surrounding areas, suggesting that reductions in NO_2 in Los Angeles significantly lowered ozone formation in the outskirts, while increases in Tehran lead to higher PO_3 .

We error characterized both systematic and random errors associated with PO_3 DNN for both OMI and TROPOMI-based products. We showed that total errors range from 25% to over 200%, with smaller errors in polluted areas. Random errors are minor on monthly-basis, with OMI exhibiting larger errors due to row anomaly issues. Systematic errors exceed 90% of the total error, primarily driven by MINDS conversion factors. The total errors budget emphasizes on the role of model used for converting satellite-based VCDs to near-surface concentrations and its importance for precisely determining ozone precursors levels near to the surface.

We developed a novel product aimed at enhancing our understanding of the variability in PO_3 and its interactions with NO_x and VOCs on a global scale. This advanced algorithm has undergone meticulous tuning and training using an extensive dataset derived from a reliable box model, which is further constrained by intensive atmospheric composition campaigns conducted by NASA and NOAA. The algorithm not only yields accurate estimates of PO_3 with minimal bias in comparison to observationally-constrained values but also facilitates the derivation of PO_3 in relation to HCHO and NO_2 . However, as indicated by Souri et al. (2025), there remain several opportunities for further improvement, including: i) the incorporation of heterogeneous chemistry; ii) consideration of the impact of partially cloudy regions and aerosols on photolysis rates; iii) the inclusion of more sophisticated chemical mechanisms for the generation of the training dataset; and iv) enhanced representation of vertical profiles of NO_2 and HCHO using observationally-constrained chemical transport models. Some of these enhancements present significant challenges, particularly the fine-resolution three-dimensional characterization of aerosol and cloud properties on a global scale, which is not obtainable with current reanalysis data. However, with the advent of newer satellite technologies such as PACE and MAIA, there may be opportunities to improve the representation of atmospheric models with respect to cloud and aerosol characteristics.

The emergence of novel geosynchronous orbit (GEO) technologies is becoming increasingly important for monitoring the daylight hourly variability in ozone precursors. In particular, the finer spatial and temporal resolution offered by the Tropospheric Emissions: Monitoring of Pollution (TEMPO), Geostationary Environment Monitoring Spectrometer (GEMS), and Sentinel-4 instruments will aid in distinguishing exceptional events from typical atmospheric conditions. In light of the success of emission mitigation strategies over high income countries, the occurrences of elevated PO_3 are becoming more infrequent, thereby necessitating a more detailed and rapid observational strategy for monitoring such events. This presents a timely opportunity to address ozone exceedance events using TEMPO in conjunction with our PO_3 estimator, especially since the algorithm is designed to handle light-limited conditions—such as those encountered during early morning and late afternoon periods when TEMPO collects data—conditions that are not feasible to analyze via the FNR approach.

Appendix A: The sensitivity maps are the directional derivative

To demonstrate that the sensitivity calculation of PO_3 to its inputs resembles (Eq.5) a directional derivative output, we can approximate the perturbations in the PO_3 DNN (denoted as $f(x)$, where x is the targeted sensitivity parameter) using the Taylor expansion:

$$f(1.1x) \approx f(x) + (1.1x - x)\nabla f(x) = f(x) + 0.1x \cdot \nabla f(x) \quad (12)$$

$$f(0.9x) \approx f(x) + (0.9x - x)\nabla f(x) = f(x) - 0.1x \cdot \nabla f(x) \quad (13)$$

The sensitivity calculation presented in Eq.3 can be rewritten in the following form:



$$S = \frac{(f(x) + 0.1\nabla f(x)) - (f(x) - 0.1\nabla f(x))}{0.2} = \frac{0.2x \cdot \nabla f(x)}{0.2} = x \cdot \nabla f(x) \quad (14)$$

Therefore, the first-order approximation of the DNN prediction, when using the given sensitivity calculation, is $x \cdot \nabla f(x)$ which represents the first-order Taylor expansion term that describes how the output changes with respect to both the gradient and the magnitude of x (i.e., directional derivative).

Appendix B. MINDS conversion factor validation

We validate the column conversion factors obtained from the MINDS simulations against corresponding values derived from aircraft spirals from several suborbital missions. The concentrations of HCHO and NO₂ in both datasets are collocated in time and space and are resampled onto a common vertical grid, ranging from the near surface up to 450 hPa in 20 hPa increments. To determine the conversion factors, these resampled concentrations are averaged within the PBL and then divided by the vertically integrated partial columns from the surface to 450 hPa. The PBLH is based on the MINDS simulations. Figure B.1 displays scatterplots of the paired conversion factor binned at 12:15 LST and 15:15 LST (±45 minutes around the TROPOMI/OMI local revisit time) for NO₂ and HCHO, respectively. The unit for these conversion factors is ppbv/col, where col represents 1×10^{15} molec.cm⁻². The comparison shows a good level of agreement between the two datasets for both species ($R^2 > 0.7$). The MINDS simulations perform slightly better for NO₂ than for HCHO. This performance difference may arise from the fact that HCHO is mainly a secondary product, meaning various uncertain VOC emissions, along with uncertain chemical processes in the model, could pile up leading to discrepancies in the vertical distribution of simulated HCHO compared to observations. Furthermore, HCHO vertical profiles can be easily affected by local circulation patterns that are difficult to resolve in coarse models (Souri et al., 2023b). We observe consistent model performance across various campaigns, except for DISCOVER-AQ Colorado. This discrepancy may result from complex topography and wind conditions in that region that the model might not fully capture. The differences between the two datasets can also be attributed to sources of error beyond the model deficiencies. For instance, the MINDS simulations represent a quarter-degree averaged concentration, which differs from the localized air samples derived from aircraft, known as the spatial representation error (Souri et al., 2022).

To account for the systematic errors resulting from the MINDS simulation in our error budget, we assign $e_{conv-HCHO}$ and $e_{conv-NO_2}$ in Eq.5 to RMSE values obtained from the comparison. The choice of RMSE is based on the fact that it contains information about the bias and the dispersion of MINDS with respect to the observations. We assume these errors to be invariant by time or location, mainly because of limited aircraft spirals ($N=57$) we have from the suborbital missions.

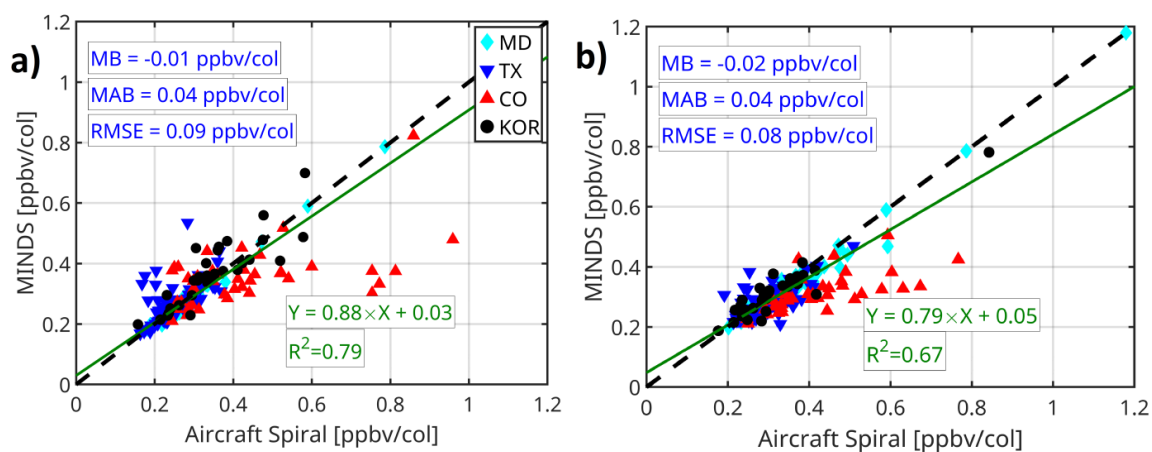


Figure B.1. The scatterplot of the column to the PBL conversion factor for (a) NO_2 and (b) HCHO obtained from aircraft spirals (x-axis) and MINDS simulation (y-axis) at the same time and location from four different suborbital missions. These 57 spirals are limited to OMI/TROPOMI overpass ± 45 min buffering time. “col” denotes 1×10^{15} molec. cm^{-2} .



961 **Financial Support**

962 This study is funded by NASA's ACMAP/Aura project (grant no. 80NSSC23K1250).

963 **Data Availability**

964 The PO₃ products can be obtained from <https://www.ozonrates.space>.

965 TROPOMI satellite data are derived from copernicus Sentinel-5P (processed by ESA), 2021, TROPOMI
966 Level 2 Nitrogen Dioxide total column products. Version 02. European Space Agency.
967 <https://doi.org/10.5270/S5P-9bnp8q8>, and copernicus Sentinel-5P (processed by ESA), 2020, TROPOMI
968 Level 2 Formaldehyde Total Column products. Version 02. European Space Agency.
969 <https://doi.org/10.5270/S5P-vgl1i7t0>. The TROPOMI UV DLER can be obtained from
970 https://www.temis.nl/surface/albedo/tropomi_ler.php (last access: 10 Nov 2024). OMI SAO HCHO at
971 https://waps.cfa.harvard.edu/sao_atmos/data/omi_hcho/OMI-HCHO-L2/ (last access, 15 Feb 2025).
972 MINDS simulations can be obtained from https://portal.nccs.nasa.gov/datashare/merra2_gmi/gmi-minds/
973 (last access, 10 April 2025). OMI NO₂ (QA4ECV) can be downloaded from <https://www.temis.nl/> (last
974 access, 10 April 2025).

975 **Competing interests**

976 Bryan N. Duncan is a member of the editorial board of Atmospheric Chemistry and Physics

977 **Acknowledgements**

978 Resources supporting this work were provided by the NASA High-End Computing (HEC) Program through
979 the NASA Center for Climate Simulation (NCCS) at Goddard Space Flight Center.

980 **Authors' contributions**

981 AHS designed and implemented the research idea, analyzed the data, made all figures except for Figures 3
982 and 4, and wrote the manuscript. GG implemented, designed, and validated the DNN algorithm, and made
983 Figures 3 and 4. LDM provided the MINDS simulations. BND helped with the interpretation of the results
984 and editing.

985

986

987



988 References

- 989 Abadi, M., Barham, P., Chen, J., Chen, Z., Davis, A., Dean, J., Devin, M., Ghemawat, S., Irving, G., Isard,
990 M., Kudlur, M., Levenberg, J., Monga, R., Moore, S., Murray, D. G., Steiner, B., Tucker, P.,
991 Vasudevan, V., Warden, P., Wicke, M., Yu, Y., and Zheng, X.: TensorFlow: A system for large-scale
992 machine learning, <https://doi.org/10.48550/arXiv.1605.08695>, 31 May 2016.
- 993 Anderson, D. C., Duncan, B. N., Liu, J., Nicely, J. M., Strode, S. A., Follette-Cook, M. B., Souri, A. H.,
994 Ziemke, J. R., González-Abad, G., and Ayazpour, Z.: Trends and Interannual Variability of the
995 Hydroxyl Radical in the Remote Tropics During Boreal Autumn Inferred From Satellite Proxy
996 Data, *Geophys. Res. Lett.*, 51, e2024GL108531, <https://doi.org/10.1029/2024GL108531>, 2024.
- 997 Ayazpour, Z., González Abad, G., Nowlan, C. R., Sun, K., Kwon, H.-A., Chan Miller, C., Chong, H., Wang,
998 H., Liu, X., Chance, K., O'Sullivan, E., Zhu, L., Vigouroux, C., De Smedt, I., Stremme, W.,
999 Hannigan, J. W., Notholt, J., Sun, X., Palm, M., Petri, C., Strong, K., Röhling, A. N., Mahieu, E.,
1000 Smale, D., Té, Y., Morino, I., Murata, I., Nagahama, T., Kivi, R., Makarova, M., Jones, N.,
1001 Sussmann, R., and Zhou, M.: Aura Ozone Monitoring Instrument (OMI) Collection 4
1002 Formaldehyde Products, *Earth Space Sci.*, 12, e2024EA003792,
1003 <https://doi.org/10.1029/2024EA003792>, 2025.
- 1004 Bates, K. H. and Jacob, D. J.: An Expanded Definition of the Odd Oxygen Family for Tropospheric Ozone
1005 Budgets: Implications for Ozone Lifetime and Stratospheric Influence, *Geophys. Res. Lett.*, 47,
1006 e2019GL084486, <https://doi.org/10.1029/2019GL084486>, 2020.
- 1007 Bauwens, M., Stavrakou, T., Müller, J.-F., De Smedt, I., Van Roozendaal, M., van der Werf, G. R.,
1008 Wiedinmyer, C., Kaiser, J. W., Sindelarova, K., and Guenther, A.: Nine years of global hydrocarbon
1009 emissions based on source inversion of OMI formaldehyde observations, *Atmos. Chem. Phys.*, 16,
1010 10133–10158, <https://doi.org/10.5194/acp-16-10133-2016>, 2016.
- 1011 Bocquet, M., Elbern, H., Eskes, H., Hirtl, M., Žabkar, R., Carmichael, G. R., Flemming, J., Inness, A.,
1012 Pagowski, M., Pérez Camacho, J. L., Saide, P. E., San Jose, R., Sofiev, M., Vira, J., Baklanov, A.,
1013 Carnevale, C., Grell, G., and Seigneur, C.: Data assimilation in atmospheric chemistry models:
1014 current status and future prospects for coupled chemistry meteorology models, *Atmos. Chem.*
1015 *Phys.*, 15, 5325–5358, <https://doi.org/10.5194/acp-15-5325-2015>, 2015.
- 1016 Boersma, K. F., Eskes, H. J., Richter, A., De Smedt, I., Lorente, A., Beirle, S., van Geffen, J. H. G. M.,
1017 Zara, M., Peters, E., Van Roozendaal, M., Wagner, T., Maasakkers, J. D., van der A, R. J.,
1018 Nightingale, J., De Rudder, A., Irie, H., Pinardi, G., Lambert, J.-C., and Compennolle, S. C.:
1019 Improving algorithms and uncertainty estimates for satellite NO₂ retrievals: results from the quality
1020 assurance for the essential climate variables (QA4ECV) project, *Atmos. Meas. Tech.*, 11, 6651–
1021 6678, <https://doi.org/10.5194/amt-11-6651-2018>, 2018.
- 1022 Brune, W. H., Miller, D. O., Thames, A. B., Allen, H. M., Apel, E. C., Blake, D. R., Bui, T. P., Commane,
1023 R., Crounse, J. D., Daube, B. C., Diskin, G. S., DiGangi, J. P., Elkins, J. W., Hall, S. R., Hanisco,
1024 T. F., Hannun, R. A., Hints, E. J., Hornbrook, R. S., Kim, M. J., McKain, K., Moore, F. L., Neuman,
1025 J. A., Nicely, J. M., Peischl, J., Ryerson, T. B., St. Clair, J. M., Sweeney, C., Teng, A. P., Thompson,
1026 C., Ullmann, K., Veres, P. R., Wennberg, P. O., and Wolfe, G. M.: Exploring Oxidation in the
1027 Remote Free Troposphere: Insights From Atmospheric Tomography (ATom), *J. Geophys. Res.-*
1028 *Atmos.*, 125, e2019JD031685, <https://doi.org/10.1029/2019JD031685>, 2020.
- 1029 Brune, W. H., Miller, D. O., Thames, A. B., Brosius, A. L., Barletta, B., Blake, D. R., Blake, N. J., Chen,
1030 G., Choi, Y., Crawford, J. H., Digangi, J. P., Diskin, G., Fried, A., Hall, S. R., Hanisco, T. F., Huey,
1031 G. L., Hughes, S. C., Kim, M., Meinardi, S., Montzka, D. D., Pusede, S. E., Schroeder, J. R., Teng,
1032 A., Tanner, D. J., Ullmann, K., Walega, J., Weinheimer, A., Wisthaler, A., and Wennberg, P. O.:



- 1033 Observations of atmospheric oxidation and ozone production in South Korea, *Atmos. Environ.*,
1034 269, 118854, <https://doi.org/10.1016/j.atmosenv.2021.118854>, 2022.
- 1035 Cazorla, M. and Brune, W. H.: Measurement of Ozone Production Sensor, *Atmos. Meas. Tech.*, 3, 545–555,
1036 <https://doi.org/10.5194/amt-3-545-2010>, 2010.
- 1037 Cazorla, M., Brune, W. H., Ren, X., and Lefer, B.: Direct measurement of ozone production rates in Houston
1038 in 2009 and comparison with two estimation methods, *Atmos. Chem. Phys.*, 12, 1203–1212,
1039 <https://doi.org/10.5194/acp-12-1203-2012>, 2012.
- 1040 Chatfield, R. B., Ren, X., Brune, W., and Schwab, J.: Controls on urban ozone production rate as indicated
1041 by formaldehyde oxidation rate and nitric oxide, *Atmos. Environ.*, 44, 5395–5406,
1042 <https://doi.org/10.1016/j.atmosenv.2010.08.056>, 2010.
- 1043 Chin, M., Ginoux, P., Kinne, S., Torres, O., Holben, B. N., Duncan, B. N., Martin, R. V., Logan, J. A.,
1044 Higurashi, A., and Nakajima, T.: Tropospheric Aerosol Optical Thickness from the GOCART
1045 Model and Comparisons with Satellite and Sun Photometer Measurements, *J. Atmos. Sci.*, 59, 461–
1046 483, [https://doi.org/10.1175/1520-0469\(2002\)059<0461:TAOTFT>2.0.CO;2](https://doi.org/10.1175/1520-0469(2002)059<0461:TAOTFT>2.0.CO;2), 2002.
- 1047 Choi, Y. and Souri, A. H.: Chemical condition and surface ozone in large cities of Texas during the last
1048 decade: Observational evidence from OMI, CAMS, and model analysis, *Remote Sens. Environ.*,
1049 168, 90–101, <https://doi.org/10.1016/j.rse.2015.06.026>, 2015a.
- 1050 Choi, Y. and Souri, A. H.: Seasonal behavior and long-term trends of tropospheric ozone, its precursors and
1051 chemical conditions over Iran: A view from space, *Atmos. Environ.*, 106, 232–240,
1052 <https://doi.org/10.1016/j.atmosenv.2015.02.012>, 2015b.
- 1053 Choi, Y., Kim, H., Tong, D., and Lee, P.: Summertime weekly cycles of observed and modeled NO_x and
1054 O₃ concentrations as a function of satellite-derived ozone production sensitivity and land use types
1055 over the Continental United States, *Atmos. Chem. Phys.*, 12, 6291–6307,
1056 <https://doi.org/10.5194/acp-12-6291-2012>, 2012.
- 1057 Compernelle, S., Verhoelst, T., Pinardi, G., Granville, J., Hubert, D., Keppens, A., Niemeijer, S., Rino, B.,
1058 Bais, A., Beirle, S., Boersma, F., Burrows, J. P., De Smedt, I., Eskes, H., Goutail, F., Hendrick, F.,
1059 Lorente, A., Pazmino, A., Pithers, A., Peters, E., Pommereau, J.-P., Remmers, J., Richter, A., van
1060 Geffen, J., Van Roozendael, M., Wagner, T., and Lambert, J.-C.: Validation of Aura-OMI QA4ECV
1061 NO₂ climate data records with ground-based DOAS networks: the role of measurement and
1062 comparison uncertainties, *Atmos. Chem. Phys.*, 20, 8017–8045, <https://doi.org/10.5194/acp-20-8017-2020>, 2020.
- 1064 David, L. M. and Nair, P. R.: Tropospheric column O₃ and NO₂ over the Indian region observed by Ozone
1065 Monitoring Instrument (OMI): Seasonal changes and long-term trends, *Atmos. Environ.*, 65, 25–
1066 39, <https://doi.org/10.1016/j.atmosenv.2012.09.033>, 2013.
- 1067 De Smedt, I., Pinardi, G., Vigouroux, C., Compernelle, S., Bais, A., Benavent, N., Boersma, F., Chan, K.-
1068 L., Donner, S., Eichmann, K.-U., Hedelt, P., Hendrick, F., Irie, H., Kumar, V., Lambert, J.-C.,
1069 Langerock, B., Lerot, C., Liu, C., Loyola, D., Pithers, A., Richter, A., Rivera Cárdenas, C., Romahn,
1070 F., Ryan, R. G., Sinha, V., Theys, N., Vlietinck, J., Wagner, T., Wang, T., Yu, H., and Van
1071 Roozendael, M.: Comparative assessment of TROPOMI and OMI formaldehyde observations and
1072 validation against MAX-DOAS network column measurements, *Atmos. Chem. Phys.*, 21, 12561–
1073 12593, <https://doi.org/10.5194/acp-21-12561-2021>, 2021.
- 1074 Demetillo, M. A. G., Anderson, J. F., Geddes, J. A., Yang, X., Najacht, E. Y., Herrera, S. A., Kabasares, K.
1075 M., Kotsakis, A. E., Lerdau, M. T., and Pusede, S. E.: Observing Severe Drought Influences on



- 1076 Ozone Air Pollution in California, *Environ. Sci. Technol.*, 53, 4695–4706,
1077 <https://doi.org/10.1021/acs.est.8b04852>, 2019.
- 1078 Duncan, B. N., Strahan, S. E., Yoshida, Y., Steenrod, S. D., and Livesey, N.: Model study of the cross-
1079 tropopause transport of biomass burning pollution, *Atmos. Chem. Phys.*, 7, 3713–3736,
1080 <https://doi.org/10.5194/acp-7-3713-2007>, 2007.
- 1081 Duncan, B. N., Yoshida, Y., Damon, M. R., Douglass, A. R., and Witte, J. C.: Temperature dependence of
1082 factors controlling isoprene emissions, *Geophys. Res. Lett.*, 36,
1083 <https://doi.org/10.1029/2008GL037090>, 2009.
- 1084 Duncan, B., Y. Yoshida, J. Olson, S. Sillman, C. Retscher, R. Martin, L. Lamsal, Y. Hu, K. Pickering, C.
1085 Retscher, D. Allen, and J. Crawford, Application of OMI observations to a space-based indicator
1086 of NO_x and VOC controls on surface ozone formation, *Atmos. Environ.*, 44, 2213–2223,
1087 <https://doi.org/10.1016/j.atmosenv.2010.03.010>, 2010.
- 1088 Eskes, H. J. and Boersma, K. F.: Averaging kernels for DOAS total-column satellite retrievals, *Atmos.*
1089 *Chem. Phys.*, 3, 1285–1291, <https://doi.org/10.5194/acp-3-1285-2003>, 2003.
- 1090 Fleming, Z. L., Doherty, R. M., von Schneidmesser, E., Malley, C. S., Cooper, O. R., Pinto, J. P., Colette,
1091 A., Xu, X., Simpson, D., Schultz, M. G., Lefohn, A. S., Hamad, S., Moolla, R., Solberg, S., and
1092 Feng, Z.: Tropospheric Ozone Assessment Report: Present-day ozone distribution and trends
1093 relevant to human health, *Elem. Sci. Anth.*, 6, 12, <https://doi.org/10.1525/elementa.273>, 2018.
- 1094 Gaudel, A., Cooper, O. R., Ancellet, G., Barret, B., Boynard, A., Burrows, J. P., Clerbaux, C., Coheur, P.-
1095 F., Cuesta, J., Cuevas, E., Doniki, S., Dufour, G., Ebojie, F., Foret, G., Garcia, O., Granados-Muñoz,
1096 M. J., Hannigan, J. W., Hase, F., Hassler, B., Huang, G., Hurtmans, D., Jaffe, D., Jones, N.,
1097 Kalabokas, P., Kerridge, B., Kulawik, S., Latter, B., Leblanc, T., Le Flochmoën, E., Lin, W., Liu,
1098 J., Liu, X., Mahieu, E., McClure-Begley, A., Neu, J. L., Osman, M., Palm, M., Petetin, H.,
1099 Petropavlovskikh, I., Querel, R., Rahpoe, N., Rozanov, A., Schultz, M. G., Schwab, J., Siddans, R.,
1100 Smale, D., Steinbacher, M., Tanimoto, H., Tarasick, D. W., Thouret, V., Thompson, A. M., Trickl,
1101 T., Weatherhead, E., Wespes, C., Worden, H. M., Vigouroux, C., Xu, X., Zeng, G., and Ziemke, J.:
1102 Tropospheric Ozone Assessment Report: Present-day distribution and trends of tropospheric ozone
1103 relevant to climate and global atmospheric chemistry model evaluation, *Elem. Sci. Anth.*, 6, 39,
1104 <https://doi.org/10.1525/elementa.291>, 2018.
- 1105 Geddes, J. A., Pusede, S. E., and Wong, A. Y. H.: Changes in the Relative Importance of Biogenic Isoprene
1106 and Soil NO_x Emissions on Ozone Concentrations in Nonattainment Areas of the United States, *J.*
1107 *Geophys. Res.-Atmos.*, 127, e2021JD036361, <https://doi.org/10.1029/2021JD036361>, 2022.
- 1108 Georgoulas, A. K., Boersma, K. F., van Vliet, J., Zhang, X., van der A, R., Zanis, P., and de Laat, J.:
1109 Detection of NO₂ pollution plumes from individual ships with the TROPOMI/S5P satellite sensor,
1110 *Environ. Res. Lett.*, 15, 124037, <https://doi.org/10.1088/1748-9326/abc445>, 2020.
- 1111 Gonzalez Abad, G., Souri, A. H., Bak, J., Chance, K., Flynn, L. E., Krotkov, N. A., Lamsal, L., Li, C., Liu,
1112 X., Miller, C. C., Nowlan, C. R., Suleiman, R., and Wang, H.: Five decades observing Earth's
1113 atmospheric trace gases using ultraviolet and visible backscatter solar radiation from space, *J.*
1114 *Quant. Spectrosc. Ra.*, 238, 106478, <https://doi.org/10.1016/j.jqsrt.2019.04.030>, 2019.
- 1115 Granier, C., Bessagnet, B., Bond, T., D'Angiola, A., Denier van der Gon, H., Frost, G. J., Heil, A., Kaiser,
1116 J. W., Kinne, S., Klimont, Z., Kloster, S., Lamarque, J.-F., Lioussé, C., Masui, T., Meleux, F.,
1117 Mieville, A., Ohara, T., Raut, J.-C., Riahi, K., Schultz, M. G., Smith, S. J., Thompson, A., van
1118 Aardenne, J., van der Werf, G. R., and van Vuuren, D. P.: Evolution of anthropogenic and biomass



- 1119 burning emissions of air pollutants at global and regional scales during the 1980–2010 period, *Clim.*
1120 *Change*, 109, 163, <https://doi.org/10.1007/s10584-011-0154-1>, 2011.
- 1121 Guenther, A. B., Jiang, X., Heald, C. L., Sakulyanontvittaya, T., Duhl, T., Emmons, L. K., and Wang, X.:
1122 The Model of Emissions of Gases and Aerosols from Nature version 2.1 (MEGAN2.1): an extended
1123 and updated framework for modeling biogenic emissions, *Geosci. Model Dev.*, 5, 1471–1492,
1124 <https://doi.org/10.5194/gmd-5-1471-2012>, 2012.
- 1125 Ichoku, C. and Ellison, L.: Global top-down smoke-aerosol emissions estimation using satellite fire
1126 radiative power measurements, *Atmos. Chem. Phys.*, 14, 6643–6667, [https://doi.org/10.5194/acp-](https://doi.org/10.5194/acp-14-6643-2014)
1127 14-6643-2014, 2014.
- 1128 Jeon, W., Choi, Y., Souri, A. H., Roy, A., Diao, L., Pan, S., Lee, H. W., and Lee, S.-H.: Identification of
1129 chemical fingerprints in long-range transport of burning induced upper tropospheric ozone from
1130 Colorado to the North Atlantic Ocean, *Sci. Total Environ.*, 613–614, 820–828,
1131 <https://doi.org/10.1016/j.scitotenv.2017.09.177>, 2018.
- 1132 Jin, X., Fiore, A. M., Murray, L. T., Valin, L. C., Lamsal, L. N., Duncan, B., Folkert Boersma, K., De Smedt,
1133 I., Abad, G. G., Chance, K., and Tonnesen, G. S.: Evaluating a Space-Based Indicator of Surface
1134 Ozone-NO_x-VOC Sensitivity Over Midlatitude Source Regions and Application to Decadal
1135 Trends, *J. Geophys. Res.-Atmos.*, 122, 10,439–10,461, <https://doi.org/10.1002/2017JD026720>,
1136 2017.
- 1137 Johnson, M. S., Philip, S., Meech, S., Kumar, R., Sorek-Hamer, M., Shiga, Y. P., and Jung, J.: Insights into
1138 the long-term (2005–2021) spatiotemporal evolution of summer ozone production sensitivity in the
1139 Northern Hemisphere derived with the Ozone Monitoring Instrument (OMI), *Atmos. Chem. Phys.*,
1140 24, 10363–10384, <https://doi.org/10.5194/acp-24-10363-2024>, 2024.
- 1141 Kingma, D. P. and Ba, J.: Adam: A Method for Stochastic Optimization,
1142 <https://doi.org/10.48550/arXiv.1412.6980>, 30 January 2017.
- 1143 Kleinman, L. I., Daum, P. H., Imre, D., Lee, Y.-N., Nunnermacker, L. J., Springston, S. R., Weinstein-Lloyd,
1144 J., and Rudolph, J.: Ozone production rate and hydrocarbon reactivity in 5 urban areas: A cause of
1145 high ozone concentration in Houston, *Geophys. Res. Lett.*, 29, 105-1-105-4,
1146 <https://doi.org/10.1029/2001GL014569>, 2002.
- 1147 Kleinman, L. I., Daum, P. H., Lee, Y.-N., Nunnermacker, L. J., Springston, S. R., Weinstein-Lloyd, J., and
1148 Rudolph, J.: A comparative study of ozone production in five U.S. metropolitan areas, *J. Geophys.*
1149 *Res.-Atmos.*, 110, <https://doi.org/10.1029/2004JD005096>, 2005.
- 1150 Martin, R. V., Fiore, A. M., and Van Donkelaar, A.: Space-based diagnosis of surface ozone sensitivity to
1151 anthropogenic emissions, *Geophys. Res. Lett.*, 31, <https://doi.org/10.1029/2004GL019416>, 2004.
- 1152 Mazzuca, G. M., Ren, X., Loughner, C. P., Estes, M., Crawford, J. H., Pickering, K. E., Weinheimer, A. J.,
1153 and Dickerson, R. R.: Ozone production and its sensitivity to NO_x and VOCs: results from the
1154 DISCOVER-AQ field experiment, Houston 2013, *Atmos. Chem. Phys.*, 16, 14463–14474,
1155 <https://doi.org/10.5194/acp-16-14463-2016>, 2016.
- 1156 Miller, D. O. and Brune, W. H.: Investigating the Understanding of Oxidation Chemistry Using 20 Years of
1157 Airborne OH and HO₂ Observations, *J. Geophys. Res.-Atmos.*, 127, e2021JD035368,
1158 <https://doi.org/10.1029/2021JD035368>, 2022.
- 1159 Mills, G., Pleijel, H., Malley, C. S., Sinha, B., Cooper, O. R., Schultz, M. G., Neufeld, H. S., Simpson, D.,
1160 Sharps, K., Feng, Z., Gerosa, G., Harmens, H., Kobayashi, K., Saxena, P., Paoletti, E., Sinha, V.,
1161 and Xu, X.: Tropospheric Ozone Assessment Report: Present-day tropospheric ozone distribution



- 1162 and trends relevant to vegetation, *Elem. Sci. Anth.*, 6, 47, <https://doi.org/10.1525/elementa.302>,
1163 2018.
- 1164 Miyazaki, K., Bowman, K. W., Yumimoto, K., Walker, T., and Sudo, K.: Evaluation of a multi-model, multi-
1165 constituent assimilation framework for tropospheric chemical reanalysis, *Atmos. Chem. Phys.*, 20,
1166 931–967, <https://doi.org/10.5194/acp-20-931-2020>, 2020.
- 1167 Molod, A., Takacs, L., Suarez, M., and Bacmeister, J.: Development of the GEOS-5 atmospheric general
1168 circulation model: evolution from MERRA to MERRA2, *Geosci. Model Dev.*, 8, 1339–1356,
1169 <https://doi.org/10.5194/gmd-8-1339-2015>, 2015.
- 1170 Nielsen, J. E., Pawson, S., Molod, A., Auer, B., da Silva, A. M., Douglass, A. R., Duncan, B., Liang, Q.,
1171 Manyin, M., Oman, L. D., Putman, W., Strahan, S. E., and Wargan, K.: Chemical Mechanisms and
1172 Their Applications in the Goddard Earth Observing System (GEOS) Earth System Model, *J. Adv.*
1173 *Model. Earth Syst.*, 9, 3019–3044, <https://doi.org/10.1002/2017MS001011>, 2017.
- 1174 Nowlan, C. R., González Abad, G., Kwon, H.-A., Ayazpour, Z., Chan Miller, C., Chance, K., Chong, H.,
1175 Liu, X., O’Sullivan, E., Wang, H., Zhu, L., De Smedt, I., Jaross, G., Seftor, C., and Sun, K.: Global
1176 Formaldehyde Products From the Ozone Mapping and Profiler Suite (OMPS) Nadir Mappers on
1177 Suomi NPP and NOAA-20, *Earth Space Sci.*, 10, e2022EA002643,
1178 <https://doi.org/10.1029/2022EA002643>, 2023.
- 1179 Opacka, B., Stavrou, T., Müller, J.-F., De Smedt, I., van Geffen, J., Marais, E. A., Horner, R. P., Millet,
1180 D. B., Wells, K. C., and Guenther, A. B.: Natural emissions of VOC and NO_x over Africa
1181 constrained by TROPOMI HCHO and NO₂ data using the MAGRITTEv1.1 model, *Atmos. Chem.*
1182 *Phys.*, 25, 2863–2894, <https://doi.org/10.5194/acp-25-2863-2025>, 2025.
- 1183 Orbe, C., Oman, L. D., Strahan, S. E., Waugh, D. W., Pawson, S., Takacs, L. L., and Molod, A. M.: Large-
1184 Scale Atmospheric Transport in GEOS Replay Simulations, *J. Adv. Model. Earth Syst.*, 9, 2545–
1185 2560, <https://doi.org/10.1002/2017MS001053>, 2017.
- 1186 Pinardi, G., Van Roozendaal, M., Hendrick, F., Theys, N., Abuhassan, N., Bais, A., Boersma, F., Cede, A.,
1187 Chong, J., Donner, S., Drosoglou, T., Dzhola, A., Eskes, H., Frieß, U., Granville, J., Herman, J. R.,
1188 Holla, R., Hovila, J., Irie, H., Kanaya, Y., Karagkiozidis, D., Kouremeti, N., Lambert, J.-C., Ma, J.,
1189 Peters, E., Pithers, A., Postlyakov, O., Richter, A., Remmers, J., Takashima, H., Tiefengraber, M.,
1190 Valks, P., Vlemmix, T., Wagner, T., and Wittrock, F.: Validation of tropospheric NO₂ column
1191 measurements of GOME-2A and OMI using MAX-DOAS and direct sun network observations,
1192 *Atmos. Meas. Tech.*, 13, 6141–6174, <https://doi.org/10.5194/amt-13-6141-2020>, 2020.
- 1193 Pusede, S. E., Steiner, A. L., and Cohen, R. C.: Temperature and Recent Trends in the Chemistry of
1194 Continental Surface Ozone, *Chem. Rev.*, 115, 3898–3918, <https://doi.org/10.1021/cr5006815>,
1195 2015.
- 1196 Pyrgou, A., Hadjinicolaou, P., and Santamouris, M.: Enhanced near-surface ozone under heatwave
1197 conditions in a Mediterranean island, *Sci. Rep.*, 8, 9191, [https://doi.org/10.1038/s41598-018-](https://doi.org/10.1038/s41598-018-27590-z)
1198 [27590-z](https://doi.org/10.1038/s41598-018-27590-z), 2018.
- 1199 Ren, X., van Duin, D., Cazorla, M., Chen, S., Mao, J., Zhang, L., Brune, W. H., Flynn, J. H., Grossberg,
1200 N., Lefer, B. L., Rappenglück, B., Wong, K. W., Tsai, C., Stutz, J., Dibb, J. E., Thomas Jobson, B.,
1201 Luke, W. T., and Kelley, P.: Atmospheric oxidation chemistry and ozone production: Results from
1202 SHARP 2009 in Houston, Texas, *J. Geophys. Res.-Atmos.*, 118, 5770–5780,
1203 <https://doi.org/10.1002/jgrd.50342>, 2013.
- 1204 Roberts, G., Wooster, M. J., and Lagoudakis, E.: Annual and diurnal african biomass burning temporal
1205 dynamics, *Biogeosciences*, 6, 849–866, <https://doi.org/10.5194/bg-6-849-2009>, 2009.



- 1206 Sadanaga, Y., Kawasaki, S., Tanaka, Y., Kajii, Y., and Bandow, H.: New System for Measuring the
1207 Photochemical Ozone Production Rate in the Atmosphere, *Environ. Sci. Technol.*, 51, 2871–2878,
1208 <https://doi.org/10.1021/acs.est.6b04639>, 2017.
- 1209 Schroeder, J. R., Crawford, J. H., Ahn, J.-Y., Chang, L., Fried, A., Walega, J., Weinheimer, A., Montzka, D.
1210 D., Hall, S. R., Ullmann, K., Wisthaler, A., Mikoviny, T., Chen, G., Blake, D. R., Blake, N. J.,
1211 Hughes, S. C., Meinardi, S., Diskin, G., Digangi, J. P., Choi, Y., Pusede, S. E., Huey, G. L., Tanner,
1212 D. J., Kim, M., and Wennberg, P.: Observation-based modeling of ozone chemistry in the Seoul
1213 metropolitan area during the Korea-United States Air Quality Study (KORUS-AQ), *Elem. Sci.*
1214 *Anth.*, 8, 3, <https://doi.org/10.1525/elementa.400>, 2020.
- 1215 Schroeder, J. R., Crawford, J. H., Fried, A., Walega, J., Weinheimer, A., Wisthaler, A., Müller, M.,
1216 Mikoviny, T., Chen, G., Shook, M., Blake, D. R., and Tonnesen, G. S.: New insights into the column
1217 CH₂O/NO₂ ratio as an indicator of near-surface ozone sensitivity, *J. Geophys. Res.-Atmos.*, 122,
1218 8885–8907, <https://doi.org/10.1002/2017JD026781>, 2017.
- 1219 Shen, Z., Yang, H., and Zhang, S.: Neural network approximation: Three hidden layers are enough, *Neural*
1220 *Netw.*, 141, 160–173, <https://doi.org/10.1016/j.neunet.2021.04.011>, 2021.
- 1221 Sillman, S. and He, D.: Some theoretical results concerning O₃-NO_x-VOC chemistry and NO_x-VOC
1222 indicators, *J. Geophys. Res.-Atmos.*, 107, ACH 26-1-ACH 26-15,
1223 <https://doi.org/10.1029/2001JD001123>, 2002.
- 1224 Sklaveniti, S., Locoge, N., Stevens, P. S., Wood, E., Kundu, S., and Dusanter, S.: Development of an
1225 instrument for direct ozone production rate measurements: measurement reliability and current
1226 limitations, *Atmos. Meas. Tech.*, 11, 741–761, <https://doi.org/10.5194/amt-11-741-2018>, 2018.
- 1227 Souri, A. and Gonzalez Abad, G. (2025) “ahsouri/ozonerates: Ozonerates v1.0”. Zenodo. doi:
1228 10.5281/zenodo.15076487.
- 1229 Souri, A. H., Chance, K., Sun, K., Liu, X., and Johnson, M. S.: Dealing with spatial heterogeneity in
1230 pointwise-to-gridded- data comparisons, *Atmos. Meas. Tech.*, 15, 41–59,
1231 <https://doi.org/10.5194/amt-15-41-2022>, 2022.
- 1232 Souri, A. H., Choi, Y., Jeon, W., Li, X., Pan, S., Diao, L., and Westenbarger, D. A.: Constraining NO_x
1233 emissions using satellite NO₂ measurements during 2013 DISCOVER-AQ Texas campaign,
1234 *Atmos. Environ.*, 131, 371–381, <https://doi.org/10.1016/j.atmosenv.2016.02.020>, 2016.
- 1235 Souri, A. H., Choi, Y., Jeon, W., Woo, J.-H., Zhang, Q., and Kurokawa, J.: Remote sensing evidence of
1236 decadal changes in major tropospheric ozone precursors over East Asia, *J. Geophys. Res.-Atmos.*,
1237 122, 2474–2492, <https://doi.org/10.1002/2016JD025663>, 2017.
- 1238 Souri, A. H., Duncan, B. N., Strode, S. A., Anderson, D. C., Manyin, M. E., Liu, J., Oman, L. D., Zhang,
1239 Z., and Weir, B.: Enhancing long-term trend simulation of the global tropospheric hydroxyl (TOH)
1240 and its drivers from 2005 to 2019: a synergistic integration of model simulations and satellite
1241 observations, *Atmos. Chem. Phys.*, 24, 8677–8701, <https://doi.org/10.5194/acp-24-8677-2024>,
1242 2024.
- 1243 Souri, A. H., González Abad, G., Wolfe, G. M., Verhoelst, T., Vigouroux, C., Pinardi, G., Compennolle, S.,
1244 Langerock, B., Duncan, B. N., and Johnson, M. S.: Feasibility of robust estimates of ozone
1245 production rates using a synergy of satellite observations, ground-based remote sensing, and
1246 models, *Atmos. Chem. Phys.*, 25, 2061–2086, <https://doi.org/10.5194/acp-25-2061-2025>, 2025.
- 1247 Souri, A. H., Johnson, M. S., Wolfe, G. M., Crawford, J. H., Fried, A., Wisthaler, A., Brune, W. H., Blake,
1248 D. R., Weinheimer, A. J., Verhoelst, T., Compennolle, S., Pinardi, G., Vigouroux, C., Langerock,



- 1249 B., Choi, S., Lamsal, L., Zhu, L., Sun, S., Cohen, R. C., Min, K.-E., Cho, C., Philip, S., Liu, X.,
1250 and Chance, K.: Characterization of errors in satellite-based HCHO/NO₂ tropospheric column ratios
1251 with respect to chemistry, column-to-PBL translation, spatial representation, and retrieval
1252 uncertainties, *Atmos. Chem. Phys.*, 23, 1963–1986, <https://doi.org/10.5194/acp-23-1963-2023>,
1253 2023a.
- 1254 Souri, A. H., Kumar, R., Chong, H., Golbazi, M., Knowland, K. E., Geddes, J., and Johnson, M. S.:
1255 Decoupling in the vertical shape of HCHO during a sea breeze event: The effect on trace gas
1256 satellite retrievals and column-to-surface translation, *Atmos. Environ.*, 309, 119929,
1257 <https://doi.org/10.1016/j.atmosenv.2023.119929>, 2023b.
- 1258 Souri, A. H., Nowlan, C. R., González Abad, G., Zhu, L., Blake, D. R., Fried, A., Weinheimer, A. J.,
1259 Wisthaler, A., Woo, J.-H., Zhang, Q., Chan Miller, C. E., Liu, X., and Chance, K.: An inversion of
1260 NO_x and non-methane volatile organic compound (NMVOC) emissions using satellite observations
1261 during the KORUS-AQ campaign and implications for surface ozone over East Asia, *Atmos. Chem.*
1262 *Phys.*, 20, 9837–9854, <https://doi.org/10.5194/acp-20-9837-2020>, 2020b.
- 1263 Souri, A. H., Nowlan, C. R., Wolfe, G. M., Lamsal, L. N., Chan Miller, C. E., Abad, G. G., Janz, S. J., Fried,
1264 A., Blake, D. R., Weinheimer, A. J., Diskin, G. S., Liu, X., and Chance, K.: Revisiting the
1265 effectiveness of HCHO/NO₂ ratios for inferring ozone sensitivity to its precursors using high
1266 resolution airborne remote sensing observations in a high ozone episode during the KORUS-AQ
1267 campaign, *Atmos. Environ.*, 224, 117341, <https://doi.org/10.1016/j.atmosenv.2020.117341>, 2020a.
- 1268 Stavrakou, T., Müller, J.-F., Bauwens, M., De Smedt, I., Lerot, C., Van Roozendaal, M., Coheur, P.-F.,
1269 Clerbaux, C., Boersma, K. F., van der A, R., and Song, Y.: Substantial Underestimation of Post-
1270 Harvest Burning Emissions in the North China Plain Revealed by Multi-Species Space
1271 Observations, *Sci. Rep.*, 6, 32307, <https://doi.org/10.1038/srep32307>, 2016.
- 1272 Stavrakou, T., Müller, J.-F., De Smedt, I., Van Roozendaal, M., Kanakidou, M., Vrekoussis, M., Wittrock,
1273 F., Richter, A., and Burrows, J. P.: The continental source of glyoxal estimated by the synergistic
1274 use of spaceborne measurements and inverse modelling, *Atmos. Chem. Phys.*, 9, 8431–8446,
1275 <https://doi.org/10.5194/acp-9-8431-2009>, 2009.
- 1276 Strahan, S. E., Duncan, B. N., and Hoor, P.: Observationally derived transport diagnostics for the lowermost
1277 stratosphere and their application to the GMI chemistry and transport model, *Atmos. Chem. Phys.*,
1278 7, 2435–2445, <https://doi.org/10.5194/acp-7-2435-2007>, 2007.
- 1279 Sullivan, J. T., McGee, T. J., Stauffer, R. M., Thompson, A. M., Weinheimer, A., Knote, C., Janz, S.,
1280 Wisthaler, A., Long, R., Szykman, J., Park, J., Lee, Y., Kim, S., Jeong, D., Sanchez, D., Twigg, L.,
1281 Sumnicht, G., Knepp, T., and Schroeder, J. R.: Taehwa Research Forest: a receptor site for severe
1282 domestic pollution events in Korea during 2016, *Atmos. Chem. Phys.*, 19, 5051–5067,
1283 <https://doi.org/10.5194/acp-19-5051-2019>, 2019.
- 1284 Tao, M., Fiore, A. M., Jin, X., Schiferl, L. D., Commane, R., Judd, L. M., Janz, S., Sullivan, J. T., Miller, P.
1285 J., Karambelas, A., Davis, S., Tzortziou, M., Valin, L., Whitehill, A., Civerolo, K., and Tian, Y.:
1286 Investigating Changes in Ozone Formation Chemistry during Summertime Pollution Events over
1287 the Northeastern United States, *Environ. Sci. Technol.*, 56, 15312–15327,
1288 <https://doi.org/10.1021/acs.est.2c02972>, 2022.
- 1289 Thorsen, T. J. and Fu, Q.: CALIPSO-inferred aerosol direct radiative effects: Bias estimates using ground-
1290 based Raman lidars, *J. Geophys. Res.-Atmos.*, 120, 12,209–12,220,
1291 <https://doi.org/10.1002/2015JD024095>, 2015.



- 1292 Tilstra, L. G., de Graaf, M., Trees, V. J. H., Litvinov, P., Dubovik, O., and Stammes, P.: A directional surface
1293 reflectance climatology determined from TROPOMI observations, *Atmos. Meas. Tech.*, 17, 2235–
1294 2256, <https://doi.org/10.5194/amt-17-2235-2024>, 2024.
- 1295 Valin, L. C., Russell, A. R., Hudman, R. C., and Cohen, R. C.: Effects of model resolution on the
1296 interpretation of satellite NO₂ observations, *Atmos. Chem. Phys.*, 11, 11647–11655,
1297 <https://doi.org/10.5194/acp-11-11647-2011>, 2011.
- 1298 van Geffen, J., Eskes, H., Compernelle, S., Pinardi, G., Verhoelst, T., Lambert, J.-C., Sneep, M., ter Linden,
1299 M., Ludewig, A., Boersma, K. F., and Veefkind, J. P.: Sentinel-5P TROPOMI NO₂ retrieval: impact
1300 of version v2.2 improvements and comparisons with OMI and ground-based data, *Atmos. Meas.*
1301 *Tech.*, 15, 2037–2060, <https://doi.org/10.5194/amt-15-2037-2022>, 2022.
- 1302 Veefkind, J. P., Aben, I., McMullan, K., Förster, H., de Vries, J., Otter, G., Claas, J., Eskes, H. J., de Haan,
1303 J. F., Kleipool, Q., van Weele, M., Hasekamp, O., Hoogeveen, R., Landgraf, J., Snel, R., Tol, P.,
1304 Ingmann, P., Voors, R., Kruizinga, B., Vink, R., Visser, H., and Levelt, P. F.: TROPOMI on the ESA
1305 Sentinel-5 Precursor: A GMES mission for global observations of the atmospheric composition for
1306 climate, air quality and ozone layer applications, *Remote Sens. Environ.*, 120, 70–83,
1307 <https://doi.org/10.1016/j.rse.2011.09.027>, 2012.
- 1308 Verhoelst, T., Compernelle, S., Pinardi, G., Lambert, J.-C., Eskes, H. J., Eichmann, K.-U., Fjæraa, A. M.,
1309 Granville, J., Niemeijer, S., Cede, A., Tiefengraber, M., Hendrick, F., Pazmiño, A., Bais, A.,
1310 Bazureau, A., Boersma, K. F., Bognar, K., Dehn, A., Donner, S., Elokho, A., Gebetsberger, M.,
1311 Goutail, F., Grutter de la Mora, M., Gruzdev, A., Gratsea, M., Hansen, G. H., Irie, H., Jepsen, N.,
1312 Kanaya, Y., Karagkiozidis, D., Kivi, R., Kreher, K., Levelt, P. F., Liu, C., Müller, M., Navarro
1313 Comas, M., PETERS, A. J. M., Pommereau, J.-P., Portafaix, T., Prados-Roman, C., Puentedura, O.,
1314 Querel, R., Remmers, J., Richter, A., Rimmer, J., Rivera Cárdenas, C., Saavedra de Miguel, L.,
1315 Sinyakov, V. P., Stremme, W., Strong, K., Van Roozendaal, M., Veefkind, J. P., Wagner, T.,
1316 Wittrock, F., Yela González, M., and Zehner, C.: Ground-based validation of the Copernicus
1317 Sentinel-5P TROPOMI NO₂ measurements with the NDACC ZSL-DOAS, MAX-DOAS and
1318 Pandonia global networks, *Atmos. Meas. Tech.*, 14, 481–510, [https://doi.org/10.5194/amt-14-481-](https://doi.org/10.5194/amt-14-481-2021)
1319 [2021](https://doi.org/10.5194/amt-14-481-2021), 2021.
- 1320 Vigouroux, C., Langerock, B., Bauer Aquino, C. A., Blumenstock, T., Cheng, Z., De Mazière, M., De
1321 Smedt, I., Grutter, M., Hannigan, J. W., Jones, N., Kivi, R., Loyola, D., Lutsch, E., Mahieu, E.,
1322 Makarova, M., Metzger, J.-M., Morino, I., Murata, I., Nagahama, T., Notholt, J., Ortega, I., Palm,
1323 M., Pinardi, G., Röhling, A., Smale, D., Stremme, W., Strong, K., Sussmann, R., Té, Y., van
1324 Roozendaal, M., Wang, P., and Winkler, H.: TROPOMI–Sentinel-5 Precursor formaldehyde
1325 validation using an extensive network of ground-based Fourier-transform infrared stations, *Atmos.*
1326 *Meas. Tech.*, 13, 3751–3767, <https://doi.org/10.5194/amt-13-3751-2020>, 2020.
- 1327 Vinken, G. C. M., Boersma, K. F., Jacob, D. J., and Meijer, E. W.: Accounting for non-linear chemistry of
1328 ship plumes in the GEOS-Chem global chemistry transport model, *Atmos. Chem. Phys.*, 11, 11707–
1329 11722, <https://doi.org/10.5194/acp-11-11707-2011>, 2011.
- 1330 Wolfe, G. M., Hanisco, T. F., Arkinson, H. L., Blake, D. R., Wisthaler, A., Mikoviny, T., Ryerson, T. B.,
1331 Pollack, I., Peischl, J., Wennberg, P. O., Crounse, J. D., St. Clair, J. M., Teng, A., Huey, L. G., Liu,
1332 X., Fried, A., Weibring, P., Richter, D., Walega, J., Hall, S. R., Ullmann, K., Jimenez, J. L.,
1333 Campuzano-Jost, P., Bui, T. P., Diskin, G., Podolske, J. R., Sachse, G., and Cohen, R. C.:
1334 Photochemical evolution of the 2013 California Rim Fire: synergistic impacts of reactive
1335 hydrocarbons and enhanced oxidants, *Atmos. Chem. Phys.*, 22, 4253–4275,
1336 <https://doi.org/10.5194/acp-22-4253-2022>, 2022.



- 1337 Wolfe, G. M., Marvin, M. R., Roberts, S. J., Travis, K. R., and Liao, J.: The Framework for 0-D Atmospheric
1338 Modeling (F0AM) v3.1, *Geosci. Model Dev.*, 9, 3309–3319, [https://doi.org/10.5194/gmd-9-3309-](https://doi.org/10.5194/gmd-9-3309-2016)
1339 [2016](https://doi.org/10.5194/gmd-9-3309-2016), 2016.
- 1340 Wu, W., Fu, T.-M., Arnold, S. R., Spracklen, D. V., Zhang, A., Tao, W., Wang, X., Hou, Y., Mo, J., Chen, J.,
1341 Li, Y., Feng, X., Lin, H., Huang, Z., Zheng, J., Shen, H., Zhu, L., Wang, C., Ye, J., and Yang, X.:
1342 Temperature-Dependent Evaporative Anthropogenic VOC Emissions Significantly Exacerbate
1343 Regional Ozone Pollution, *Environ. Sci. Technol.*, 58, 5430–5441,
1344 <https://doi.org/10.1021/acs.est.3c09122>, 2024.
- 1345 Yu, K., Jacob, D. J., Fisher, J. A., Kim, P. S., Marais, E. A., Miller, C. C., Travis, K. R., Zhu, L., Yantosca,
1346 R. M., Sulprizio, M. P., Cohen, R. C., Dibb, J. E., Fried, A., Mikoviny, T., Ryerson, T. B., Wennberg,
1347 P. O., and Wisthaler, A.: Sensitivity to grid resolution in the ability of a chemical transport model
1348 to simulate observed oxidant chemistry under high-isoprene conditions, *Atmos. Chem. Phys.*, 16,
1349 4369–4378, <https://doi.org/10.5194/acp-16-4369-2016>, 2016.